

Banner appropriate to article type will appear here in typeset article

Receptivity and instability of the hypersonic flow over moderately blunt cones

N. d'Eprémesnil¹†, C. Caillaud¹, G. Lehnasch², M.Olazabal¹ and P. Jordan²

¹CEA-CESTA, 15 Avenue des Sablières, CS60001, 33116 Le Barp Cedex, France

²Département Fluides, Thermique, Combustion, Institut PPRIME, CNRS – Université de Poitiers – ENSMA, UPR 3346, 86036 Poitiers, France

(Received xx; revised xx; accepted xx)

With a view to identifying and understanding the linear receptivity and amplification mechanisms that underpin laminar-to-turbulent transition over blunt bodies in hypersonic flow, we use resolvent analysis to study the flow over a blunt cone with 7° half-angle at Mach number $M_\infty = 6$, zero angle of attack, and nose-radius-based Reynolds number $Re_{R_n} = 90000$. Optimal forcing and responses are obtained for frequencies up to 330 kHz and azimuthal wavenumbers between 0 and 200. Wall-temperature effects are accounted for by considering both isothermal ($T_w = 300$ K) and adiabatic wall conditions. The resolvent analysis shows that stationary streak modes are the most amplified in the isothermal case, followed by entropy-layer modes between 20 and 140 kHz. In the adiabatic case, the 1st Mack mode is the most amplified. The entropy layer, caused by the nose-tip bluntness, has a profound influence on the receptivity structures. For the optimal streak mode, the most intense receptivity structures lie deep in the entropy layer, further away from the boundary-layer edge compared to the equivalent sharp-cone streak mode. This indicates that atmospheric disturbances may excite streak-like instability without fully penetrating the boundary layer. For the entropy-layer modes, the dominant receptivity and fluctuation signatures are located within the entropy layer. An energy-budget analysis reveals that these modes are most susceptible to kinetic disturbances and they sign the most on temperature fluctuations. These modes are found to leverage a temperature mixing mechanism that exploits the baseflow's wall-normal temperature gradient in the entropy layer to grow.

Key words: Resolvent analysis, boundary layer transition, instability, blunt hypersonic flows

1. Introduction

Hypersonic flight presents complex vehicle-design challenges. At these high-speed hypersonic flight conditions, a large amount of kinetic energy of the air flow is converted into heat which is transferred to the vehicle walls. To sustain the intense heating, most hypersonic vehicles possess both a thermal protection system (TPS) and some bluntness at the tip. In these conditions the state of the boundary layer, i.e. laminar or turbulent, has an important

† Email address for correspondence: nicolas.du-val-d-epremesnil@ensma.fr

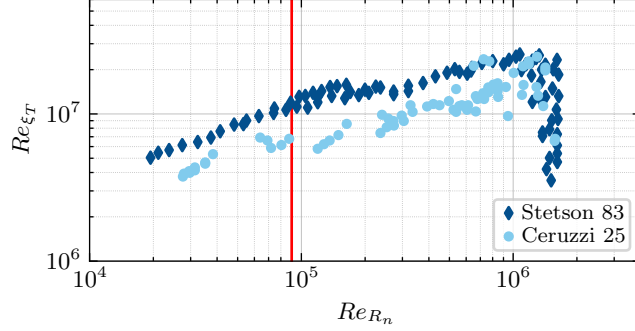


Figure 1: Reynolds number of transition versus nose radius based Reynolds number adapted from data from [Ceruzzi et al. \(2025\)](#); [Stetson et al. \(1983\)](#). The red line is Re_{R_n} of this study.

effect on the heat flux directed into the vehicle. Accurate prediction of the position of the laminar-to-turbulent transition is therefore crucial for the design optimisation of hypersonic vehicles. Poor estimation may result in either loss of the vehicle or, in the case of over-cautious design, significant additional weight associated with the heat shield ([Defense Science Board Washington Dc 1988](#)). The mechanisms underpinning transition on blunt hypersonic bodies are complex and remain poorly understood, and it is this observation that motivates the present study.

In the canonical sharp-cone case, at 0° of attack, it is understood that Mack modes are responsible for transition ([Mack 1987](#)). These are modal, convective instabilities with an exponential spatial growth rate. And traditional engineering models such as the e^N method provide satisfactory results for estimation of the transition location on canonical geometries, based on theoretical results of locally parallel Linear Stability Theory (LST). However, when bluntness increases, the Mack modes are damped and three flow-transition regimes, with respect to the nose radius, have been identified by [Stetson et al. \(1983\)](#): *small*, *moderate* and *large* bluntness regimes. These findings have been confirmed in recent experiments ([Marineau et al. 2014](#); [Jewell et al. 2018](#); [Ceruzzi et al. 2024](#)) and the transition Reynolds number is plotted in Figure 1. In the *small* bluntness case, LST predicts the transition delay due to the attenuation of Mack modes with increasing bluntness ([Rosenboom et al. 1999](#)). In the *moderate* regime, when bluntness increases further, the baseflow becomes significantly different from the sharp canonical case. The blunt nosetip introduces a detached bow shock which creates continuously changing jump conditions along the shockwave. This induces a non-uniform shock layer and an entropy layer (EL) appears above the boundary layer (BL). In this case, the transition Reynolds number becomes larger and the Mack modes are no longer responsible for transition, which occurs before the Mack-mode amplitude is large enough to cause transition ([Lei & Zhong 2012](#); [Marineau et al. 2014](#); [Paredes et al. 2019b](#)). As bluntness becomes even more important, the *large* bluntness regime is reached. In this regime, the transition Reynolds number suddenly reduces, see $Re_{R_n} > 10^6$ in Figure 1. This phenomenon is referred to as *transition reversal*. [Reshotko & Tumin \(2004\)](#) and [Paredes et al. \(2017\)](#) argue that in this regime, transient growth due to nosetip surface roughness could explain the decrease in transition Reynolds number.

The mechanisms responsible for transition, in the *moderate* and *large* bluntness regimes are not yet well understood. We thus consider linear amplification mechanisms that may arise in the *moderate* bluntness regime. Recent studies have shown that non-modal growth may explain transition ([Paredes et al. 2019a, 2020](#); [Cook et al. 2018](#)). Optimal growth theory explored in the framework of the Harmonic Linearised Navier-Stokes Equations (HLNSE)

and the Parabolised Stability Equations (PSE) has shown that substantial transient growth of streak and entropy layer modes may occur. [Paredes *et al.* \(2020\)](#) later performed Direct Numerical Simulation (DNS) at $M_\infty = 5.9$ and $Re_{R_n} = 139000$, where a pair of optimal perturbations at 250 kHz, corresponding to oblique entropy layer disturbances, were shown to produce transition through the generation of stationary streaks (via a triadic interaction of the oblique entropy layer modes) in the boundary layer. Though the initial perturbation was located in the entropy layer, the non-linear interaction led to an excitation of the boundary layer. At similar conditions, linear DNS shows larger growth associated with entropy layer perturbation than that captured by PSE analysis ([Hartman *et al.* 2021](#)) indicating that optimal PSE may miss the truly optimal linear mechanisms. Recently, schlieren visualisation ([Grossir *et al.* 2019](#); [Kennedy *et al.* 2019, 2022](#); [Ceruzzi *et al.* 2024](#)), has shown elongated wisp-like structures in the entropy layer that are qualitatively consistent with entropy layer modes found in linear analysis. This further supports the scenario of transient growth underpinned by entropy layer mechanisms in the *moderate* bluntness regime.

While entropy layer modes appear to be relevant for the transition process, it is important to explore in a systematic fashion all possible linear amplification mechanisms. To date, there has not been such a systematic study of the receptivity and response of the flow for blunt-cone geometries in this regime. Furthermore, regarding the entropy layer modes, the underlying physical mechanisms are still not well understood, and it remains unclear what type of receptivity leads to their excitation.

To address these questions, we perform a comprehensive investigation of optimal linear amplification mechanisms in hypersonic flow over a blunt conical body in the moderate bluntness regime using global resolvent analysis. It is performed over a wide range of frequencies and azimuthal wavenumbers, enabling the identification and study of optimal receptivity and amplification mechanisms. This provides an upper bound on the amplification of external perturbations via linear processes and permits identification of the mechanisms that may be triggered by environmental disturbances. To further understand the underlying physics, a detailed analysis of the dominant optimal modes is undertaken : their energy content and the associated production terms are presented and discussed.

Additionally, during flight, the wall temperature may vary between cold to adiabatic and hot wall conditions. Past research has shown that modification of the wall temperature with regard to the recovery temperature can significantly affect the linear amplification mechanisms ([Mack 1987](#)). Furthermore, flight enthalpy and pressure conditions are difficult to reach in wind tunnel tests and the run durations are often short in front of the model thermal inertia. Hence, most hypersonic wind tunnel flows usually only allow for a small range of cold-isothermal wall temperature conditions. Therefore, considering that previous numerical stability analysis conducted on the blunt cone have focused solely on such cold isothermal wall conditions, we choose to include an adiabatic wall condition in order to provide insights into the wall temperature effect on blunt cone flow instability.

The outline of the paper is as follows: Section §2 introduces the flow conditions, the geometry and the governing equations of this problem and the associated numerical framework. Section §3 presents the baseflow used for the resolvent analysis. Section §4 presents the optimal and suboptimal modes obtained through global resolvent analysis. Two families of modes stand out and are further studied in the next sections. In section §5, the optimal streak mode's energy content and production is analysed and in section §6 a similar study is conducted on entropy layer modes. Finally, section §7 discusses the effect of wall temperature through the resolvent analysis of a baseflow with an adiabatic wall. Section §8 concludes and offers perspectives for future research.

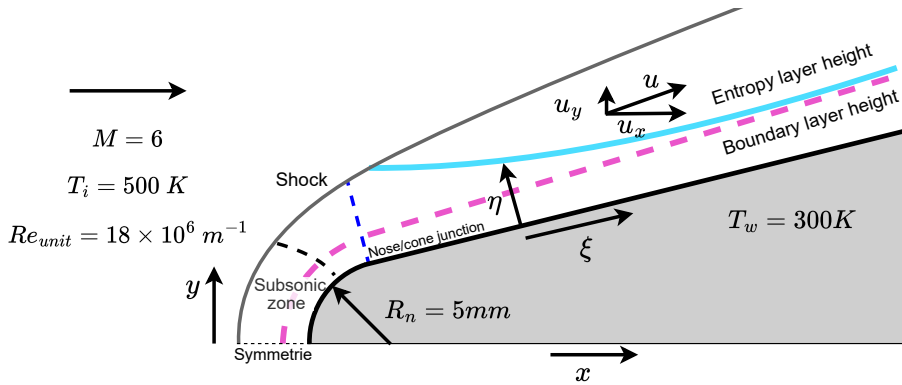


Figure 2: Scheme of the flow topology and setup

name	R_n [mm]	Re_{R_n}	Re_{unit} [m^{-1}]	$T_{i,\infty}$ [K]	M_∞	wall boundary condition
sharp isothermal	0.1	1 800	18×10^6	500	6	isothermal $T_w = 300$ K
blunt isothermal	5	90 000	18×10^6	500	6	isothermal $T_w = 300$ K
blunt adiabatic	5	90 000	18×10^6	500	6	adiabatic $\partial T / \partial \eta _{wall} = 0$ K/m

Table 1: Studied configurations

2. Numerical setup and methods

2.1. Geometry and flow conditions

We consider a blunt cone with a spherical nose radius R_n , with a conical frustum of half-angle $\alpha = 7^\circ$ and 0° angle of attack at $M = 6$. The cone is 50 cm long and is truncated at the nose by the distance necessary to fit a spherical nose of radius R_n . Figure 2 presents a schematic version of the baseflow and geometry, where ξ^* and η^* are respectively the curvilinear distance from the tip and the wall-normal distance. There are 3 cases considered, summarised in table 1.

The 5 mm nose radius case with an isothermal wall condition corresponds closely to the experiment B4 of [Kennedy et al. \(2022\)](#) performed in the AFRL Mach 6 Ludwieg tube. These conditions are transitional, and through similarity based on experiments done by [Jewell et al. \(2018\)](#) in the same wind tunnel, transition occurs at a distance of approximatively 46 cm from the tip. The B4 experiments performed by [Kennedy et al. \(2022\)](#) show through high-speed schlieren visualisation the lack of 2nd Mack mode amplification and elongated wisp-like structures in the entropy layer.

2.2. Governing equations

The flow is governed by the compressible Navier-Stokes equations, which are non-dimensionalised as follow:

$$x = \frac{x^*}{L_{ref}}, \quad \rho = \frac{\rho^*}{\rho_\infty}, \quad p = \frac{p^*}{\rho_\infty \mathbf{u}_\infty^2}, \quad \mathbf{u} = \frac{\mathbf{u}^*}{u_\infty},$$

$$\begin{aligned} T &= \frac{T^*}{T_\infty}, & \rho E &= \frac{(\rho E)^*}{\rho_\infty u_\infty^2}, & t &= \frac{t^* u_\infty}{L_{ref}}, \\ Pr &= \frac{\mu_\infty c_p}{\lambda_\infty}, & M &= \frac{u^*}{a_\infty}, & Re &= \frac{\rho_\infty u_\infty L_{ref}}{\mu_\infty}, \end{aligned} \quad (2.1)$$

where $[\rho \quad \mathbf{u} \quad p]^T$ are the usual primitive variables with $\mathbf{u} = (u_x, u_y, u_z)^T$ the Cartesian velocity vector, T the static temperature, $E = c_v T + \frac{1}{2} \mathbf{u}^2$ and λ the thermal conductivity, μ the dynamic viscosity which follows Sutherland's law, c_p and c_v the specific heat capacities and the subscript ∞ refers to unperturbed far field flow conditions and superscript $*$ denotes dimensionalised variables. L_{ref} is chosen as the nose radius (R_n) of the corresponding blunt cone. The compressible Navier-Stokes equations are used and can be written compactly as:

$$\frac{\partial \mathbf{q}}{\partial t} = \mathbf{N}(\mathbf{q}) + \mathbf{f}, \quad \mathbf{q} = [\rho \quad \rho \mathbf{u} \quad \rho E]^T, \quad (2.2)$$

where \mathbf{N} represents the Navier-Stokes operator, with the viscous stress tensor $\boldsymbol{\tau} = \mu \left(\nabla \mathbf{u} + (\nabla \mathbf{u})^T - \frac{2}{3} (\nabla \cdot \mathbf{u}) \mathbf{I} \right)$, \mathbf{I} the identity matrix, \mathbf{q} the conservative-variable vector and \mathbf{f} an external forcing modelling freestream turbulence effects, wind tunnel noise or any other disturbance source terms. A thermally and calorically perfect gas is considered with specific heat ratio $\gamma = 1.4$ and constant Prandtl number $Pr = 0.72$,

$$p = \frac{\rho T}{\gamma M_\infty^2}, \quad c_v = \frac{1}{\gamma M_\infty^2 (\gamma - 1)}. \quad (2.3)$$

2.3. Resolvent framework

As shown by past studies, investigating transition on blunt cones requires to account for the full, modal and non-modal, linear dynamics of the Navier-Stokes operator. Resolvent analysis is well suited for this, as it captures the global linear dynamics and flow receptivity to external perturbations. To investigate the linear response of the flow, the Navier-Stokes equations are linearized around a steady baseflow, fixed point of the non-linear system, i.e., $\mathbf{N}(\bar{\mathbf{q}}) = 0$. This is done by expanding the flow state in a first-order Taylor series in ε , where ε is small enough to justify the linear approximation:

$$\mathbf{q} = \bar{\mathbf{q}} + \varepsilon \mathbf{q}', \quad \mathbf{f} = \bar{\mathbf{f}} + \varepsilon \mathbf{f}' = \mathbf{0} + \varepsilon \mathbf{f}', \quad \varepsilon \ll 1, \quad (2.4)$$

$$\frac{\partial \mathbf{q}'}{\partial t} = \mathbf{J} \mathbf{q}' + \mathbf{f}', \quad (2.5)$$

with $\mathbf{J} = \left. \frac{\partial \mathbf{N}(\mathbf{q})}{\partial \mathbf{q}} \right|_{\bar{\mathbf{q}}}$, the Jacobian computed for the baseflow $\bar{\mathbf{q}}$. To study the flow receptivity and instability we look for the response \mathbf{q}' , associated with the forcing \mathbf{f}' . Considering stationarity and the zero angle of attack, the flow is homogeneous in both the azimuthal and temporal directions, the perturbation ansatz can be written,

$$\begin{aligned} \mathbf{q}'(x, r, \theta, t) &= \hat{\mathbf{q}}(x, r) e^{i(-\omega t + m\theta)} + \mathbf{c.c.}, \\ \mathbf{f}'(x, r, \theta, t) &= \hat{\mathbf{f}}(x, r) e^{i(-\omega t + m\theta)} + \mathbf{c.c.}, \end{aligned} \quad (2.6)$$

where m and $\omega = 2\pi f$ are, respectively, the azimuthal wavenumber and temporal pulsation, and $\mathbf{c.c.}$ denotes the complex conjugate. In this paper, subscript r will refer to the real part of the complex value. Injecting the ansatz 2.6 in equation 2.5 and simplifying, the linear system can be expressed in the frequency domain as:

$$\hat{\mathbf{q}} = \mathcal{R} \hat{\mathbf{f}}, \quad (2.7)$$

where $\mathcal{R} = \mathcal{R}(\omega, m) = (i\omega\mathbf{I} - \mathbf{J})^{-1}$ is the resolvent operator. The system defined by equation 2.5 is thus rewritten as an input/output problem where for every forcing $\hat{\mathbf{f}}$, at a given azimuthal wavenumber and pulsation, there is a corresponding response $\hat{\mathbf{q}}$. The ratio between forcing and response energies defines a gain:

$$\mu^2(\omega, m) = \frac{\|\hat{\mathbf{q}}\|_q}{\|\hat{\mathbf{f}}\|_f} \quad (2.8)$$

where $\|\cdot\|_x$ is the norm associated with a weighted inner product defined as $\langle \mathbf{q}, \mathbf{q} \rangle_x = \mathbf{q}^H \mathbf{W}_x \mathbf{q}$, where \mathbf{W}_x is a weight matrix. To evaluate the perturbation energy, the Chu norm (Chu 1965) is generally used for compressible flows. This energy can be written in non-dimensional form following Bugeat *et al.* (2019). In what follows, both the forcing and response norms use the respective matrix form \mathbf{W}_f and \mathbf{W}_q of the Chu norm. Optimal forcing and response can then be found by maximising the gain,

$$\mu_0^2(\omega, m) = \max_{\hat{\mathbf{f}}} \frac{\|\hat{\mathbf{q}}\|_q^2}{\|\hat{\mathbf{f}}\|_f^2} = \max_{\hat{\mathbf{f}}} \frac{\hat{\mathbf{f}}^H \mathcal{R}^H \mathbf{W}_q \mathcal{R} \hat{\mathbf{f}}}{\hat{\mathbf{f}}^H \mathbf{W}_f \hat{\mathbf{f}}}. \quad (2.9)$$

The gain defines a generalised Rayleigh quotient which is linked to the generalised hermitian eigenvalue problem:

$$\mathcal{R}^H \mathbf{W}_q \mathcal{R} \hat{\mathbf{f}} = \mu^2 \mathbf{W}_f \hat{\mathbf{f}}. \quad (2.10)$$

Solving this system is equivalent to solving for the right singular vectors of the singular value decomposition (SVD) of the weighted resolvent operator (Towne *et al.* 2018),

$$\mathcal{R}_w = \mathbf{W}_q^{1/2} \mathcal{R} \mathbf{W}_f^{-1/2} = \tilde{\mathbf{Q}} \Sigma \tilde{\mathbf{F}}^H, \quad (2.11)$$

$$\mathbf{Q} = \mathbf{W}_q^{-1/2} \tilde{\mathbf{Q}}, \quad (2.12)$$

$$\mathbf{F} = \mathbf{W}_f^{-1/2} \tilde{\mathbf{F}}. \quad (2.13)$$

By the properties of the SVD, \mathbf{Q} and \mathbf{F} form, respectively, orthonormal bases for the optimal responses $\hat{\mathbf{q}}_i$ and optimal forcings $\hat{\mathbf{f}}_i$ ordered from the most energetic mode to the least, this ordering being manifest in the gains contained in the diagonal matrix Σ . Any real forcing $\hat{\mathbf{f}}_{real}$ experienced in flight or in a wind tunnel would then be expressed as a linear combination of the optimal orthogonal forcing basis and the flow response would be a linear combination of the optimal orthogonal response basis modulated in amplitude by the gains and the inner product $\langle \hat{\mathbf{f}}_i, \hat{\mathbf{f}}_{real} \rangle$,

$$\hat{\mathbf{q}}_{real} = \sum_{i=0}^N \hat{\mathbf{q}}_i \mu_i^2 \langle \hat{\mathbf{f}}_i, \hat{\mathbf{f}}_{real} \rangle, \quad (2.14)$$

where $\hat{\mathbf{q}}_i$ and $\hat{\mathbf{f}}_i$ are respectively the i^{th} vector of the optimal response and forcing basis and μ_i^2 the associated gains. This leads to a receptivity coefficient $c_i = \mu_i^2 \langle \hat{\mathbf{f}}_i, \hat{\mathbf{f}}_{real} \rangle$ expressing how well a given external disturbance is able to bring energy to the flow response. It should be noted that in order to keep the gain values comparable between different cases in the non-dimensionalised framework, the gains can be scaled by the reference timescale.

Contrary to classical linear stability methods, such as LST or PSE, no assumption is made about the baseflow parallelism nor about the modal nature of the instability mechanisms in the streamwise direction. Resolvent modes account for the non-normality of the linear operator by definition (Schmid 2007). This allows for the exploration and ranking of linear

amplification mechanisms in the flow without constraints whether they are of modal or non-modal nature. If a modal instability exists, such as the second Mack mode, then the resolvent optimal forcing will be the structure that optimally receives energy from external sources (Equation 2.14) in order to amplify the instability, and the non-normality of the operator may be leveraged to excite the instability. The response will be the spatial structure of this mechanism, the associated gain will be very large due to the exponential modal amplification and the gain separation between leading and sub-optimal modes will be pronounced.

2.4. Numerical solver

Both the baseflow and resolvent analyses are carried out using the BROADCAST solver developed at ONERA (Poulain *et al.* 2023). The code employs a finite-volume formulation, with high-order FE-MUSCL state reconstruction at cell interfaces for the convective fluxes. In this study, a 7th-order reconstruction is used. Viscous fluxes are computed using a 4th-order compact finite difference scheme. Temporal integration of the Navier–Stokes equations begins from a uniform initial condition and is advanced using an implicit LU-SGS scheme with an approximate Jacobian until transients are eliminated. Final convergence of the steady-state baseflow is achieved through a pseudo-Newton iteration, with a convergence criterion of $\|\partial \mathbf{q} / \partial t\|_{L_2} \leq 10^{-10}$.

After obtaining the steady baseflow, the linear fluxes are obtained via algorithmic differentiation of the non-linear fluxes using the *source transformation* approach, implemented with the TAPENADE library from INRIA (Hascoet & Pascual 2013). This technique produces linearized fluxes that are exact and retain the formal accuracy of the original non-linear discretization. These linearized expressions are used to assemble the Jacobian matrix at the fixed point. Owing to the use of explicit spatial discretization schemes, the resulting Jacobian is both sparse and accurate, making it well suited for the global resolvent analysis.

2.4.1. Boundary conditions

BROADCAST uses ghost cells to impose all the boundary conditions on the flow. Supersonic inflow is imposed with a Dirichlet condition in the far field. Axisymmetric conditions are imposed on the axis of axisymmetry. Outflow is imposed with a 0th order extrapolation at the supersonic outlet. Finally, isothermal or adiabatic wall viscous boundary conditions are imposed on all surfaces.

2.5. Meshing of the numerical domain

The domain of interest is the (O, x, r) half plane of the blunt cone with an axisymmetric condition. The grid construction procedure follows the previous convergence studies done in Caillaud *et al.* (2025b). The mesh is structured and curvilinear and is constructed from mesh-refinement laws imposed on the wall, the shock line, and the far field line in the streamwise direction. In the wall normal direction, the mesh-refinement laws are imposed on the axisymmetry line, the sphere cone junction, and the outlet. A transfinite interpolation is applied to construct the complete mesh. The height of the first cell at the wall is set to 0.25 times the value of a y^+ criteria based on the laminar skin friction. About 120 cells are present in the boundary layer. The imposed shock line on the mesh is a spline found in an iterative manner until the shock line is sufficiently well aligned with the physical shock such that numerical convergence of the fixed point ensues.

3. Baseflow

The blunt geometry creates a detached, curved bow shock in front of the object. This generates a continuous range of Rankine-Hugoniot jump conditions where the entropy varies, thus

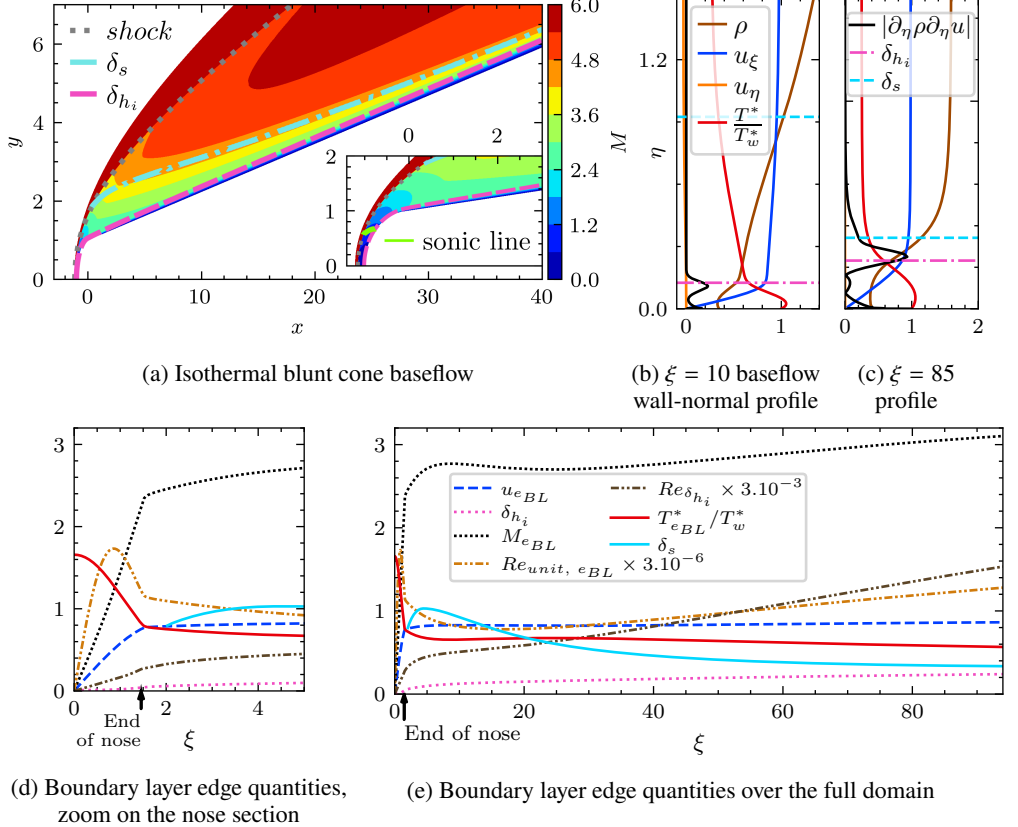


Figure 3

creating an entropy layer. Figure 3a displays the Mach number over the isothermal blunt cone where the detached shock is visible along with the entropy layer and boundary layer heights. Velocity also varies in the entropy layer, as can be seen in Figures 3b, 3c, rendering any definition of the boundary and entropy layer heights delicate. To remain consistent with the literature, definitions from Paredes *et al.* (2019b) are used where the boundary layer height (δ_{h_i}) is determined by the minimum height to the wall where the total enthalpy reaches 99.5% of its freestream value: $h_i(\delta_{h_i}) = 0.995h_{i,\infty}$. Similarly, the entropy layer height (δ_s) is defined as the minimum height to the wall for which the entropy difference to the freestream is equal to 25% of its value at the wall : $\Delta s(\delta_s) = 0.25\Delta s_{wall}$, where $\Delta s(x) = s(x) - s_\infty$.

The conditions along the upper limit of the boundary layer are plotted in Figures 3d & 3e. On the nose section, the evolutions of the quantities is fast. The Mach number starts at zero at the stagnation point and increases to about 2.2 at the end of the sphere, crossing the sonic line at $\xi = 0.72$. Due to the strong favourable pressure gradient, the boundary layer remains thin over the nose and begins to grow further downstream. It reaches a maximum at the end of the domain of $\delta_{h_i} = 0.24$. With the chosen definition for entropy layer height, the upper limit is only reached after $\xi = 2$. The edge of the entropy layer reaches a maximum at $\xi = 4.5$ with $\delta_s = 1.03$ before decreasing and asymptotically converging towards the boundary layer height.

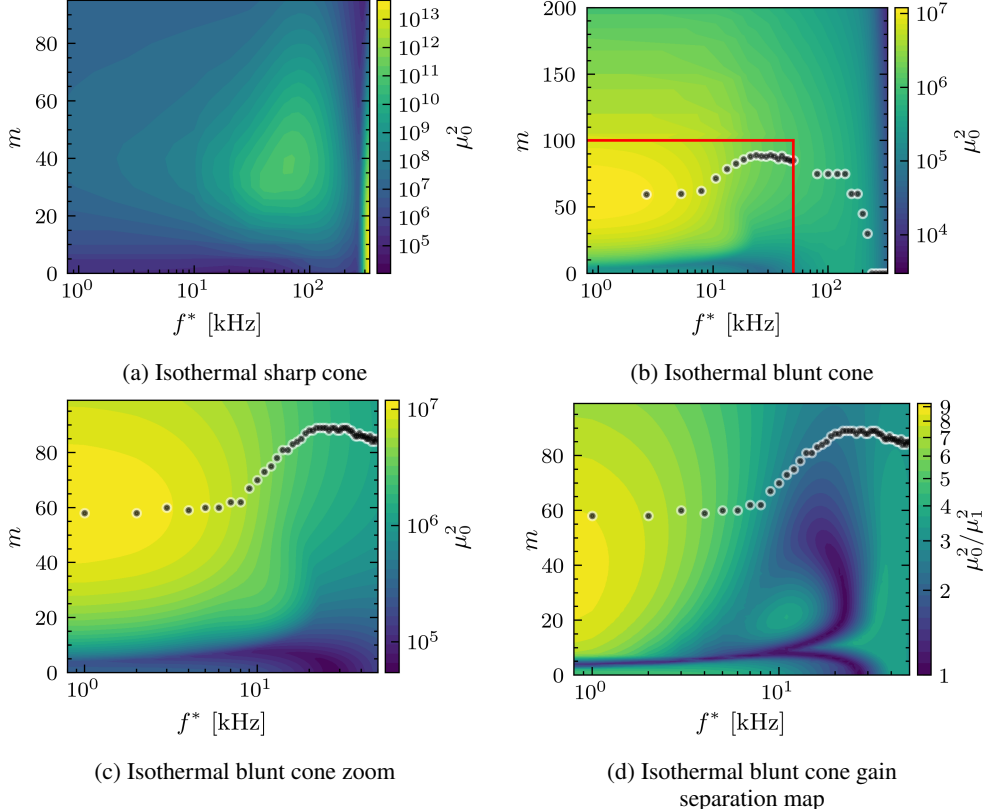


Figure 4: Isothermal gain maps in the (f^*, m) plane. ● most amplified mode at given f^*

4. Isothermal resolvent gain maps

A first way to obtain an overview of the dominant amplification mechanisms is to look at optimal gain maps $\mu_0^2(f^*, m)$. This section presents results for the isothermal blunt-cone case and uses a classical sharp cone as a reference to assess the effect of bluntness. Figures 4a, 4b show the optimal gain map μ_0^2 in the frequency-azimuthal wavenumber plane (f^*, m) for frequencies between 0 and 330 kHz and azimuthal wavenumber ranging from 0 to 100 in the sharp reference and up to 200 for the blunt case. The resolvent analysis reveals a stark difference between sharp and blunt cases. Firstly, the maximum gain for the blunt case is more than 6 orders of magnitude smaller than the sharp case. This large difference can be attributed to the already known strong attenuation of the modal Mack modes, and more specifically the 2nd Mack mode, due to bluntness. In the sharp case, this mode is most amplified for $(f^*, m) = (330 \text{ kHz}, 0)$ and corresponds to the most amplified mode in the computed (f^*, m) plane. The attenuation in the blunt case is due to the lower local Reynolds number caused by the entropy layer (Lei & Zhong 2012) which weakens the density gradient subduing the acoustic resonance which the second mode uses to amplify Batista *et al.* (2020), and is consistent with experiments performed by Marineau *et al.* (2014). In this analysis, the 2nd mode is so strongly attenuated in the blunt case that it no longer exists as an optimal resolvent mode (see Appendix A for more details about mesh convergence). The dynamics shift from being dominated by a lower-rank high-frequency mechanisms to a predominantly higher-rank system where the most amplified modes are at lower frequencies. Figure 4c shows a zoom between $f^* \in [0, 50]$ kHz and $m \in [0, 100]$ of the gain map corresponding to

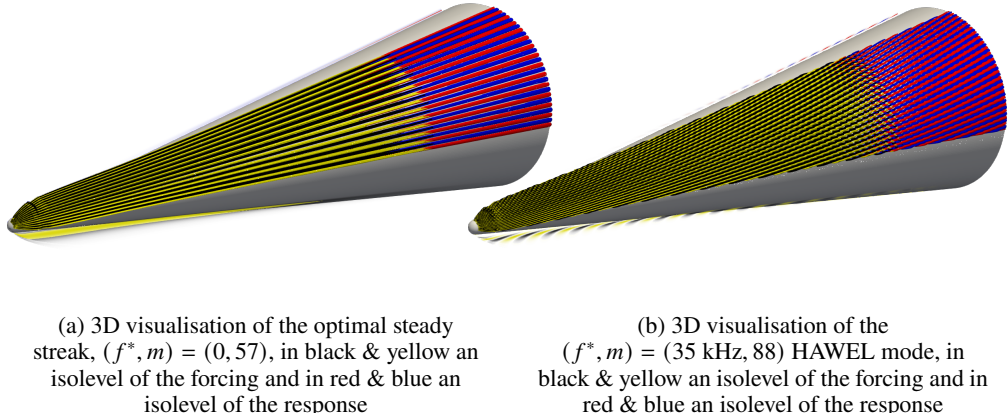


Figure 5

the red rectangle in Figure 4b. Figure 4d presents the corresponding gain separation between the optimal mode and the first suboptimal mode, expressed as the ratio μ_0^2/μ_1^2 .

The family of most amplified modes correspond to streaks at $f^* = 0$ kHz with the most amplified at $m = 57$ (Figure 5a) with gain $\mu_0^2 \approx 10^7 \text{ s}^2$, and gain separation around 9. This is consistent with the PSE analysis of [Paredes et al. \(2019a\)](#), which finds streaks to be the most amplified mode in a configuration close to ours. This mode will be discussed in detail later, in section 5.

The most amplified mode as a function of frequency, given by the black dots, shifts towards higher azimuthal wavenumber as frequency increases and reaches a maximum of $m = 89$ at $f^* = 21$ kHz. The azimuthal wavenumber of the most amplified mode remains high up to $f^* = 140$ kHz before dropping to zero. These modes between 20 kHz and 140 kHz have a strong forcing and response support in the entropy layer and will be referred to as high-azimuthal-wavenumber-entropy-layer modes (HAWEL) (Figure 5b). These results further agree with [Paredes et al. \(2019a\)](#) who observed a strong amplification of entropy layer modes. The gain separation for this family of modes ranges between 2 and 4 as can be seen in Figure 4d. The gain of the most amplified mode decreases with frequency, as shown in Figure 6. For the frequency range corresponding to HAWEL modes, the gain is 6 to 20 times less than the optimal streak mode. However, entropy layer wisps have been observed experimentally ([Grossir et al. 2019](#); [Kennedy et al. 2022](#); [Ceruzzi et al. 2024](#)), motivating a thorough investigation of their properties, which we present in Section 6.

In the gain separation map, Figure 4d, a local peak appears at $(f^*, m) = (11 \text{ kHz}, 21)$. The optimal mode at this position corresponds to the 1st Mack mode, which can be recognised by the characteristic forcing and response profiles (see Figure 24, in Appendix B). As mentioned, due to the change in baseflow induced by bluntness, the first Mack modes are significantly damped and shifted to lower frequencies and azimuthal wavenumbers compared to the sharp cone case, where the most amplified first Mack mode occurs at $(f^*, m) = (65 \text{ kHz}, 37)$.

4.1. Suboptimal modes

The higher-order nature of the blunt cone flow regime, (i.e. lower gain separation), in comparison with the low-order modal mechanisms associated with the sharp cone, motivates a more detailed review of the suboptimal resolvent response and forcing modes. In this section, the gain separation is discussed for different azimuthal wavenumbers and the associated response and forcing structures are investigated.

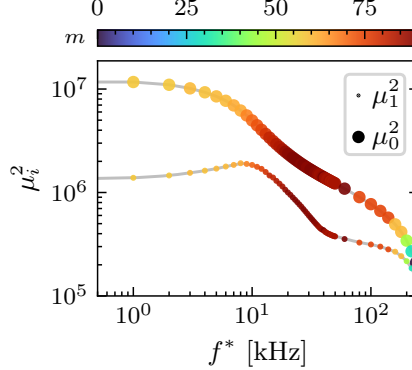


Figure 6: Optimal and 1st suboptimal gain functions for the most amplified modes as function of frequency for the isothermal blunt case

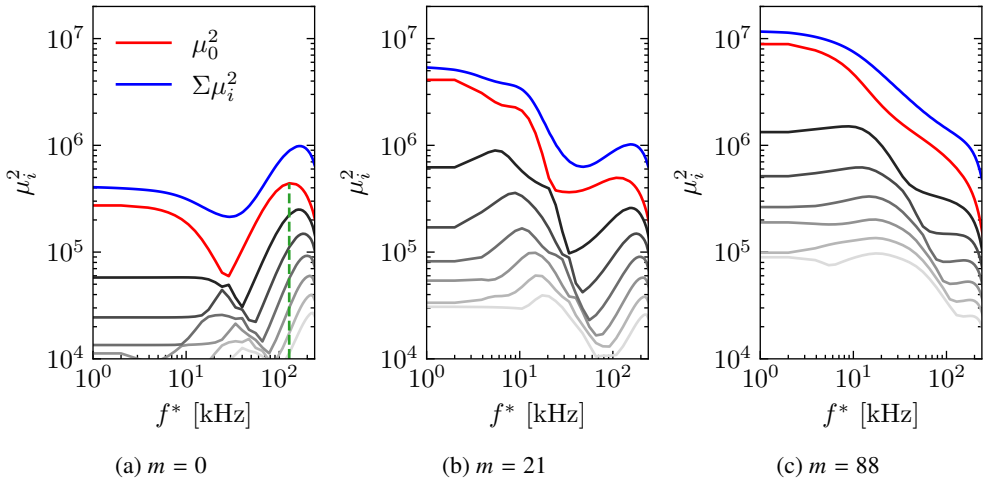


Figure 7: Optimal gain and first few suboptimal gains as function of f for different m

In Figure 7 is presented the gain functions of the first few optimal modes at different azimuthal wavenumbers. Starting at $m = 88$, the gains of the first two optimal modes are presented in Figure 7c. Figure 8 shows the profiles of the first two optimal modes at different frequencies at $\xi = 20$ for the forcing and at the end of the domain for the response. At low frequency, the most amplified mode is a suboptimal streak (the optimal being at $m = 57$). This is observable with the characteristic shape of the forcing structure with wall-normal and azimuthal velocity forcing and a strong response on streamwise velocity and temperature. The key characteristics for the optimal streaks will be discussed in more detail in section 5.

As the frequency increases (Figure 7c), the gain diminishes and the forcing structure moves into the entropy layer for both the optimal and suboptimal modes : these are the HAWEL modes. At $f^* = 128$ kHz, the forcing signs most strongly on $f_{\hat{u}_\theta}$ and $f_{\hat{u}_\xi}$ and the response responds strongly on temperature in the entropy layer. The difference between the optimal and suboptimal mode is the presence of a two lobe structure in the forcing, however the response profiles are quite similar. A more detailed analysis of HAWEL modes will be done in section 6.

Now considering the modes at $m = 0$, see Figure 7a, there appear to be two clear

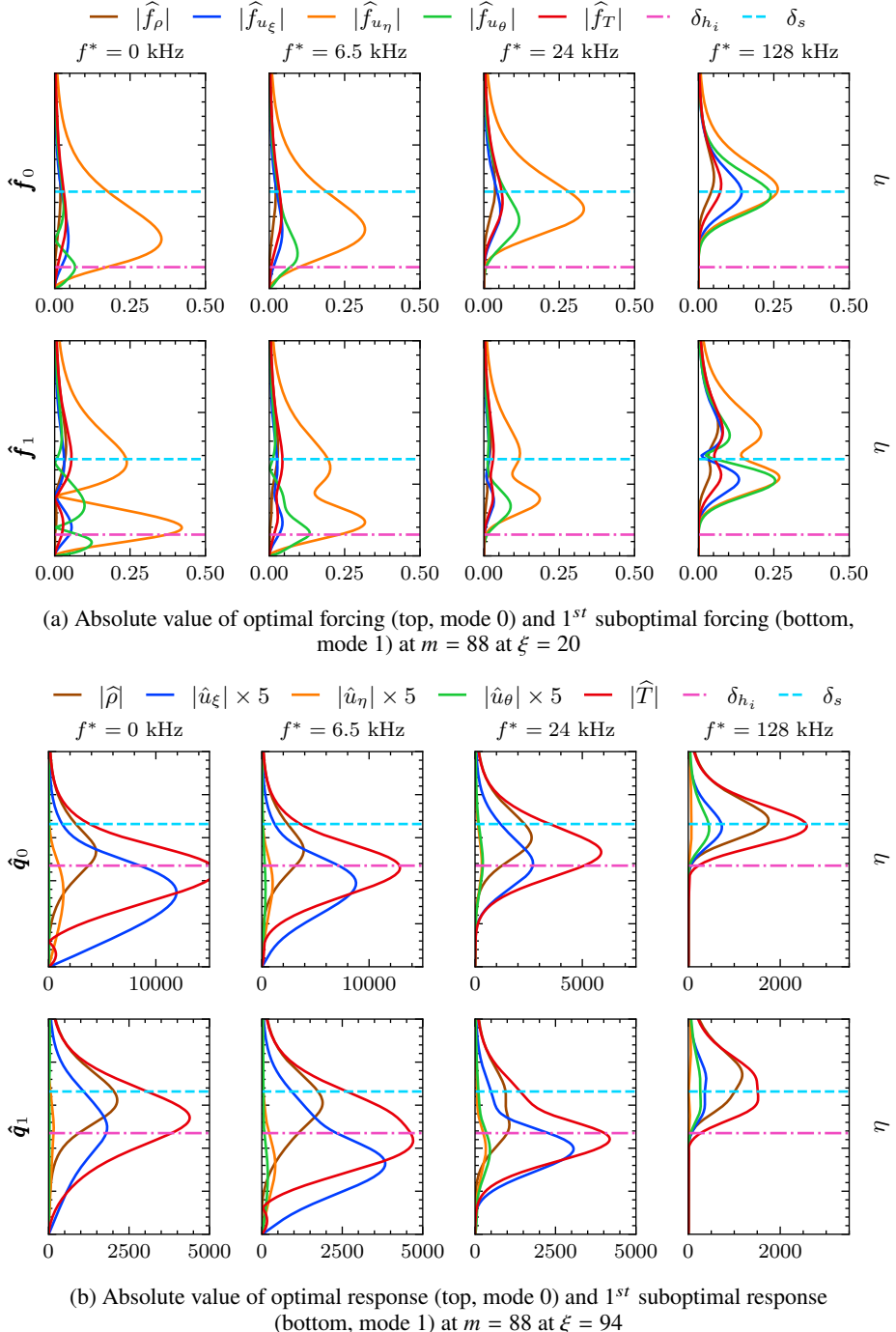


Figure 8

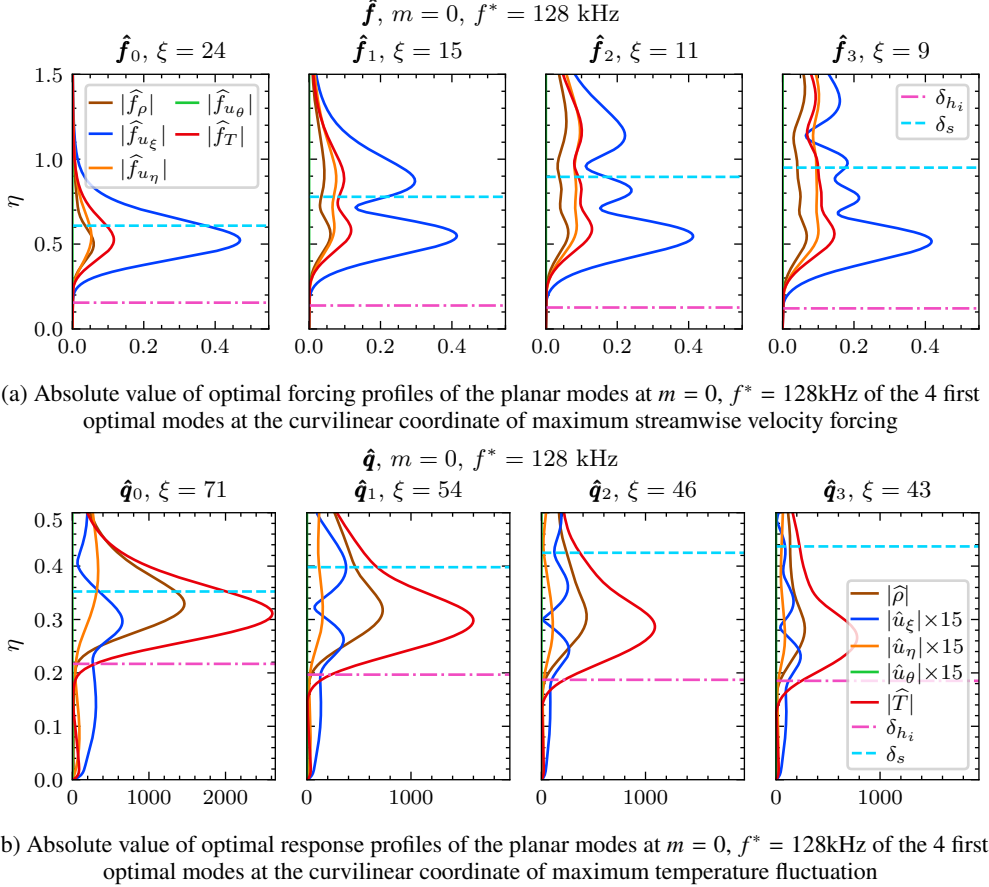


Figure 9

mechanisms switching dominant position at $f^* = 25$ kHz. The gain for the lower frequency region ($f^* \leq 10$ kHz) correspond to a weak mechanism that has a signature at the shock, suggesting some spurious modes (see Appendix B). At higher frequencies, the dominant mechanism switches and the new optimal mode peaks at $f^* = 128$ kHz and signs in the entropy layer. Figure 9 shows the wall-normal profiles of the first 4 optimal modes at 128 kHz, following the green dashed line in Figure 7a. The streamwise position of these modes is the position at which there is maximum amplitude in the streamwise velocity forcing and temperature response which are the dominant primitive variables of these modes. All these modes have a forcing and response signature in the entropy layer. As the mode order increases, both the peak forcing and response position move upstream. Though these modes sign in the entropy layer they have characteristics different from HAWEL modes that distinguishes them : the most intense forcing variable is on streamwise velocity forcing contrary to HAWEL modes where it is a combination of wall-normal and azimuthal velocity forcing.

At $m = 21$, see Figure 7b, there is again a shift in optimal mechanism. At low frequency the optimal mode is a streak. When the frequency increases the optimal mode becomes the 1st Mack mode and has the largest gain separation around $f^* = 11$ kHz. At $f^* = 20$ kHz there is a switch in dominant amplification mechanism. These new modes have maximum gain near $f^* = 130$ kHz and have similar characteristics compared to the ($f^* = 128$ kHz, $m = 0$) modes but have increased azimuthal velocity forcing. These modes between 25 kHz and

	Streaks	1st-mode	LAWEL	HAWEL
Frequency range [kHz]	[0, 5]	[7, 20]	[70, 250]	[20, 140]
m range	[40, 80]	[15, 35]	[0, 20]	broad $m_{peak} \approx 90$
Gain [s^2]	$\sim 10^7$	$\sim 2.10^6$	$\sim 4.10^5$	[$6.10^5, 2.10^6$]
Maximum gain separation	≈ 10	≈ 5	≈ 4	≈ 4

Table 2: Summary of the main mechanisms

240 kHz and at low azimuthal wavenumber seem to be oblique version of the planar modes earlier discussed and will be referred to as Low Azimuthal Wavenumber Entropy Layer modes (LAWEL), see Appendix B for more details.

A summary of these mechanisms main features is provided in Table 2. The next sections will focus on the description and analysis of the mechanisms associated with the growth of the dominant optimal modes, starting with the optimal streak mode.

5. Isothermal blunt cone optimal streak mode

The overall most amplified mode for a unit forcing energy corresponds to a steady streak mode at $f^* = 0$ kHz and $m = 57$. In order to explore the characteristics of this streak mode in comparison with sharp cone flows, an analysis of the Chu energy is conducted. This energy norm is defined as

$$E_{Chu} = \frac{1}{2} \int_V \underbrace{\bar{\rho} |\mathbf{u}'|^2}_{\text{Kinetic (KE)}} + \underbrace{\frac{\bar{T}}{\bar{\rho} \gamma M^2} \rho'^2}_{\text{Density term (D)}} + \underbrace{\frac{\bar{\rho}}{(\gamma - 1) \gamma M^2 \bar{T}} T'^2}_{\text{Temperature term (T)}} dV, \quad (5.1)$$

which consists of a kinetic energy (KE) term, a density term (D) and a temperature term (T). The wall-normal integrated Chu energy density ($E_\eta(\xi) = \int_0^{\eta_{max}} E(\xi, \eta) d\eta$) is shown in Figure 10a. It shows where and how the Chu energy density is distributed for both the forcing and the response. The forcing energy density comprises only kinetic energy, the temperature fluctuation T and density fluctuation D energy terms being negligible. The wall-normal-integrated energy density of the forcing in the nose section is very small, and it strongly increases at the beginning of the cone, peaking at $\xi = 10$, which is slightly after the maximum separation between the entropy layer and boundary layer limits. The response is maximum at the end of the domain where it is comprised of kinetic energy fluctuations associated with streamwise streaks, but with a strong contribution from the T energy term. Figure 10b, shows the contribution of the different velocity terms to the kinetic energy. The forcing is initially almost entirely dominated by the wall-normal velocity fluctuations, up to around $\xi = 50$ where the kinetic energy of the azimuthal velocity component becomes comparable. This later part is the signature of a forcing structure that has taken the form of longitudinal vorticity; but it is interesting that in the upstream region of maximum forcing, the optimal motion involves a strong radial fluctuation localised in the entropy layer. For the response, it is the streamwise component of the kinetic energy which is most important.

The forcing and response structures are shown in the (ξ, η) streamwise plane in Figure 11 for the most energetic Chu norm components: \hat{f}_{u_η} and \hat{u}_ξ . Additionally, to get a better picture of how the mode is organised, multiple (η, θ) cross-sections at different axial positions are shown in Figure 12 for both forcing and response. These figures show the forcing velocity

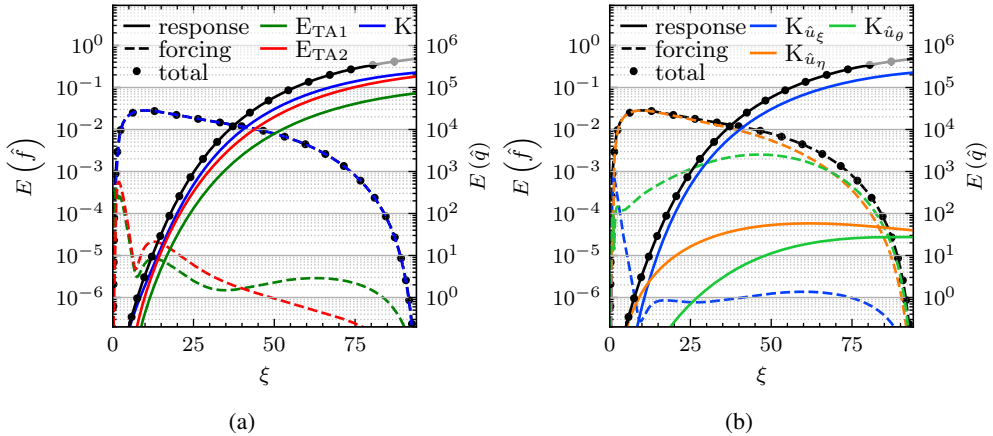


Figure 10: Wall-normal integrated Chu energy density (E_η) (left) and kinetic energy density (right) as function of ξ of the streak mode

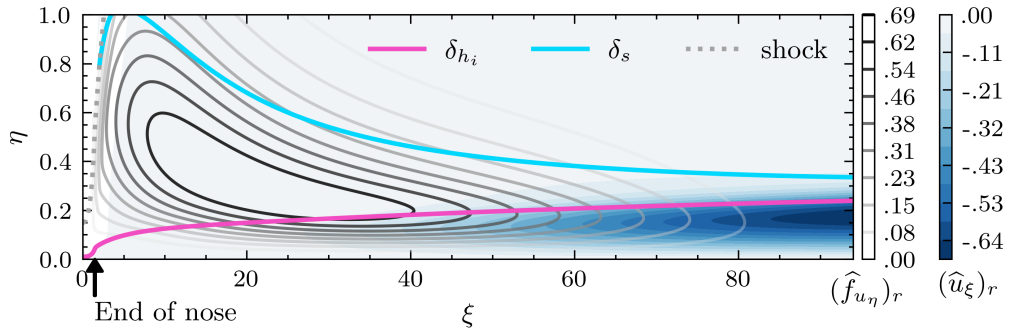


Figure 11: Global shape of the real parts of the wall-normal velocity forcing (grey) and streamwise velocity response (blue) corresponding to variables with the largest amplitudes in the streak mode. Normalised by their respective maximum absolute value

field and the associated streamwise vorticity, computed as $\hat{\mathbf{f}}_{\omega, \xi} = \partial \hat{\mathbf{f}}_\theta / \partial \eta - \partial \hat{\mathbf{f}}_\eta / \partial \theta$, at two upstream positions where the forcing is strong; and the response velocity vector field further downstream.

Initially, the forcing is dominated by almost purely wall-normal velocity fluctuations which are primarily localised in the entropy layer, and are composed of adjacent azimuthal segments with opposed wall normal velocity. At these upstream stations, indeed where receptivity is maximal (peak in forcing), the mechanism has many features comparable with the lift-up mechanism, but a key difference lies in the dominant forcing support being localised in the entropy layer which lies well above the boundary layer in the upstream region. This highlights the importance of the entropy layer in the generation of streaks for blunt bodies. And it provides an indication that atmospheric disturbances traversing the bow shock can excite streak-like disturbances within the boundary layer without necessarily penetrating as far as the boundary layer. The downstream evolution of forcing and response illustrate how, as the entropy layer merges with the boundary layer, the characteristic roll-streak configuration of the lift-up mechanism forms. The longitudinal-vorticity of the forcing gradually moves into the boundary layer, reinforcing the streak-like response in the boundary layer, which continues to grow with increasing streamwise position.

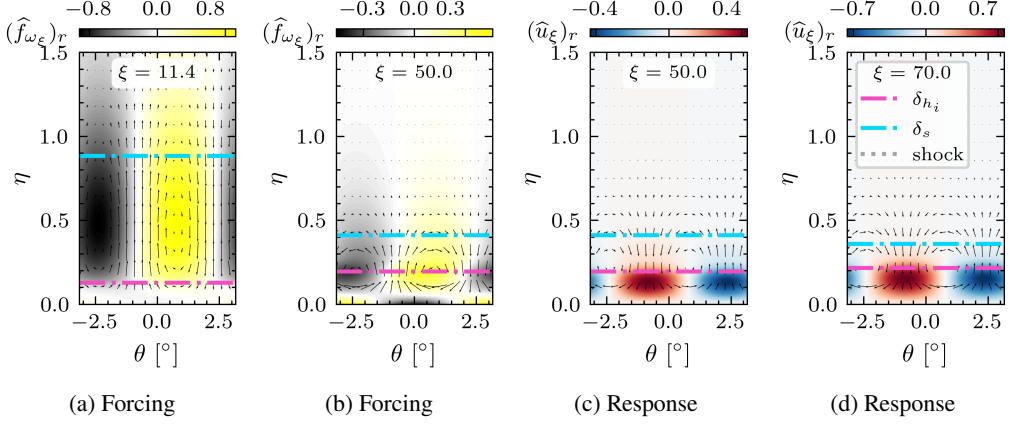


Figure 12: Real part of the forcing velocity vector field with associated streamwise vorticity (**left**) & real part of the response velocity (**right**) for the optimal streak mode

To explore the mechanisms responsible for the creation of this mode, we consider the energy budget of the linearised kinetic and temperature energy equations, similarly to [Dwivedi *et al.* \(2019\)](#). In this analysis, the energy (KE) and temperature (T) terms are decomposed into transport (Tr), production (P), source (S), viscous (V) and forcing (F) terms as following:

$$\bar{\rho} \partial_t \mathbf{u}' \cdot \mathbf{u}' \xi' \mathbf{e}_\xi + \text{KE}_{\text{Tr}, \xi} = \text{KE}_{\text{P1}, \xi} + \text{KE}_{\text{P2}, \xi} + \text{KE}_{\text{S}, \xi} + \text{KE}_{\text{F}, \xi} \quad (5.2)$$

$$\frac{\bar{\rho}}{2(\gamma - 1)\gamma M_\infty^2 \bar{T}} \partial_t T'^2 + \text{T}_{\text{Tr}} = \text{T}_I + \text{T}_{\text{II}} + \text{T}_{\text{S1}} + \text{T}_{\text{V1}} + \text{T}_{\text{V}\mu 1} + \text{T}_{\text{S2}} + \text{T}_{\text{V2}} + \text{T}_{\text{V}\mu 2} + \text{T}_{\text{F}} \quad (5.3)$$

the complete derivation of these equations is given in [Appendix C](#).

The streamline curvature is found to be small where the response is located : $1/R < 10^{-10}$, where R is local radius of curvature ([Appendix D](#)), this is why the energy budget analysis was conducted on wall-parallel lines. [Figure 13](#) presents the most significant wall-normal integrated, time and azimuthally averaged, energy budget terms as function of ξ , here are their expressions for the kinetic energy equation :

$$\text{KE}_{\text{P1}, \xi} = \left\langle -\bar{\rho} (\mathbf{u}' \cdot \nabla) \bar{\mathbf{u}} \cdot \mathbf{u}' \xi' \mathbf{e}_\xi \right\rangle = \left\langle \bar{\rho} \left(\underbrace{-u_\xi' \partial_\xi \bar{u}_\xi}_{\text{Acceleration P1}_\xi} \underbrace{-u_\eta' \partial_\eta \bar{u}_\xi}_{\text{Shear P1}_\eta} \right) \mathbf{u}' \right\rangle \quad (5.4)$$

$$\text{KE}_{\text{P2}, \xi} = \left\langle -\bar{\rho} \frac{\rho'}{\bar{\rho}} (\bar{\mathbf{u}} \cdot \nabla) \bar{\mathbf{u}} \cdot \mathbf{u}' \xi' \mathbf{e}_\xi \right\rangle \approx \left\langle \bar{\rho} \left(-\frac{\rho'}{\bar{\rho}} (\bar{\mathbf{u}} \cdot \nabla) \bar{u}_\xi \right) \mathbf{u}' \right\rangle \quad (5.5)$$

where $\langle \cdot \rangle = \frac{m_f}{2\pi} \int_0^{\eta_{\max}} \int_0^{2\pi/m} \int_0^{1/f} \cdot dt d\theta d\eta$, when $m \neq 0$ and $f \neq 0$, otherwise their respective mean is dropped.

The production terms arise from (i) the transport of baseflow velocity by velocity fluctuations, see [Equation 5.4](#), and (ii) a density fluctuation term, see [Equation 5.5](#). Since the kinetic energy of this mode is dominated by streamwise velocity fluctuations, only those are considered in this study. The first production term is further separated into two components: the first called *acceleration* is due to the streamwise acceleration or deceleration of the mean flow, and the second called *shear* is dependant on wall-normal gradient of the mean flow and resulting from the lift-up effect, ([Landahl 1980](#)). [Figure 13a](#) shows that the lift-up mechanism

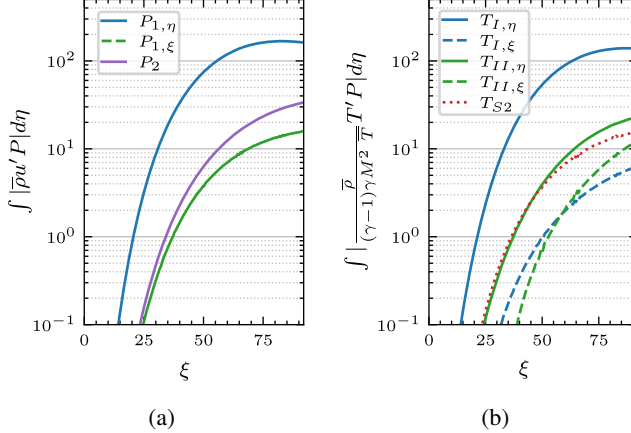


Figure 13: Wall-normal integrated dominant production terms for the linearised kinetic energy equation (left, 13a) and temperature equation (right, 13b) for the optimal streak mode

dominates and is the main mechanism through which kinetic energy is extracted from the baseflow to the mode along the whole domain.

For the T equation, the dominant terms are :

$$T_I = \left\langle -\frac{\bar{\rho}}{(\gamma - 1)\gamma M_\infty^2 \bar{T}} \mathbf{u}' \cdot (\nabla \bar{T}) \right\rangle = \left\langle -\frac{\bar{\rho}}{(\gamma - 1)\gamma M_\infty^2 \bar{T}} \left(\underbrace{u_\xi' \partial_\xi \bar{T}}_{\text{wall-parallel } T_{I,\xi}} + \underbrace{u_\eta' \partial_\eta \bar{T}}_{\text{wall-normal } T_{I,\eta}} \right) \right\rangle, \quad (5.6)$$

$$T_{II} = \left\langle -\frac{\rho'}{(\gamma - 1)\gamma M_\infty^2 \bar{T}} \bar{\mathbf{u}} \cdot (\nabla \bar{T}) \right\rangle = \left\langle -\frac{\rho'}{(\gamma - 1)\gamma M_\infty^2 \bar{T}} \left(\underbrace{\bar{u}_\xi \partial_\xi \bar{T}}_{\text{wall-parallel } T_{II,\xi}} + \underbrace{\bar{u}_\eta \partial_\eta \bar{T}}_{\text{wall-normal } T_{II,\eta}} \right) \right\rangle, \quad (5.7)$$

$$T_{S2} = \left\langle -\frac{\bar{\rho}}{\gamma^2 M_\infty^4} (\nabla \cdot \mathbf{u}') \right\rangle, \quad (5.8)$$

where T_I and T_{II} represent transport of baseflow temperature by, respectively, velocity and density fluctuations and are the analogous production terms P_1 and P_2 in the KE equation. T_{S2} is the velocity dilatation heating. Here, it is the wall-normal $T_{I,\eta}$ term that contributes the most to T energy, see Figure 13b. The wall-normal velocity response mixes the thermal boundary layer, bringing high baseflow temperature flow up and low temperature flow down, creating temperature streaks.

In conclusion, the streak receptivity mechanism of the optimal streak modes in the *moderately blunt* regime is comprised of radial velocity pumping in the entropy layer which activates: the lift-up mechanism responsible for the growth of streamwise velocity streaks and a similar mixing mechanism associated with the thermal gradient, creating temperature streaks.

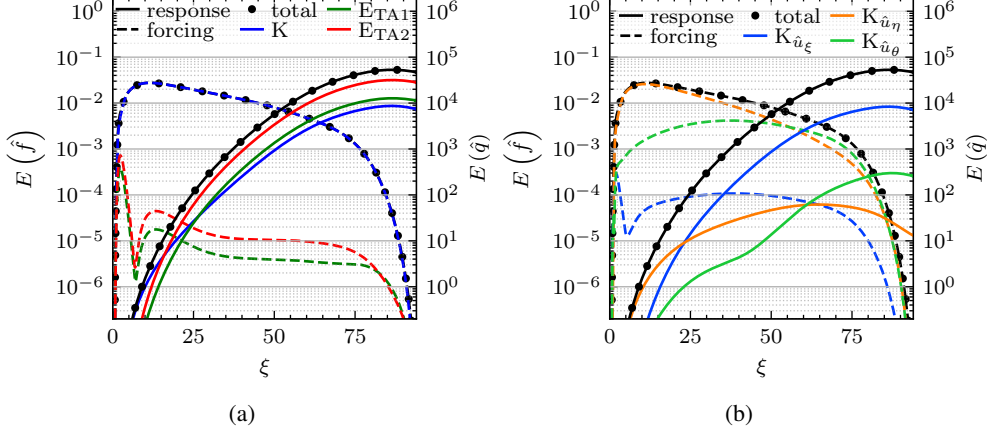


Figure 14: Wall-normal integrated Chu energy density E_η (left 14a) and kinetic energy density (right 14b) as function of ξ for the entropy layer mode

6. Isothermal blunt cone optimal HAWEL modes

While the HAWEL mode family is 6 to 20 times less amplified than the optimal streak mode, entropy layer fluctuations have been observed experimentally by [Kennedy et al. \(2022\)](#) and controlled DNS studies have shown that they may underpin transition ([Hartman et al. 2021](#); [Paredes et al. 2020](#)). Furthermore, *realisable-perturbation* resolvent analysis shows that the gain values computed by standard resolvent, as we are doing, should be considered with caution ([Kamal et al. 2023](#)). In other words, the mechanisms that will arise depend to a large degree on the kinds of perturbations entering the flow from the atmosphere and how they can project on the optimal forcing support (see Equation 2.14). This is another reason why it is important, in our study, to carefully consider all modes and mechanisms. For these reasons, a thorough characterisation of HAWEL modes is performed in this section, first on a specific example at $(f^*, m) = (35 \text{ kHz}, 88)$ and then for the family of HAWEL modes with support in the entropy layer. In the following section, we will refer to the HAWEL modes only as entropy layer modes.

6.1. Analysis of an entropy layer mode at $f^* = 35 \text{ kHz}$, $m = 88$

In this section, a detailed analysis of an entropy layer mode at $f^* = 35 \text{ kHz}$, $m = 88$ is presented. This mode is representative of the larger group of optimal entropy layer modes. And this mode in particular was chosen because it lies well within the entropy layer family mode (i.e far from other optimal mechanisms seen in the gain map Figure 4c) while being one of the most amplified entropy layer modes with a gain $\mu_0^2 = 1.7 \times 10^6 \text{ s}^2$. The nature of this mode is investigated through its energetics by first looking at its energy growth in the domain. Then the shape of this mode is presented. Finally, an energy budget analysis is carried in order to understand the sources of this energy growth.

The forcing energy E_η is predominantly comprised of kinetic energy, see Figure 14a. There is little forcing energy at the tip of the blunt nose, but it rises sharply at the beginning of the cone section and peaks at $\xi = 11.6$, close to the maximum separation between the boundary and entropy layers. The forcing energy then slowly decreases in intensity, up to $\xi = 70$ where it falls sharply. In Figure 14b, the kinetic energy density is decomposed into its three velocity components. The forcing is primarily composed of wall-normal velocity, until $\xi = 50$ where azimuthal velocity forcing becomes as important. This is a signature of longitudinal vorticity forcing. The response on the other hand is initially dominated by

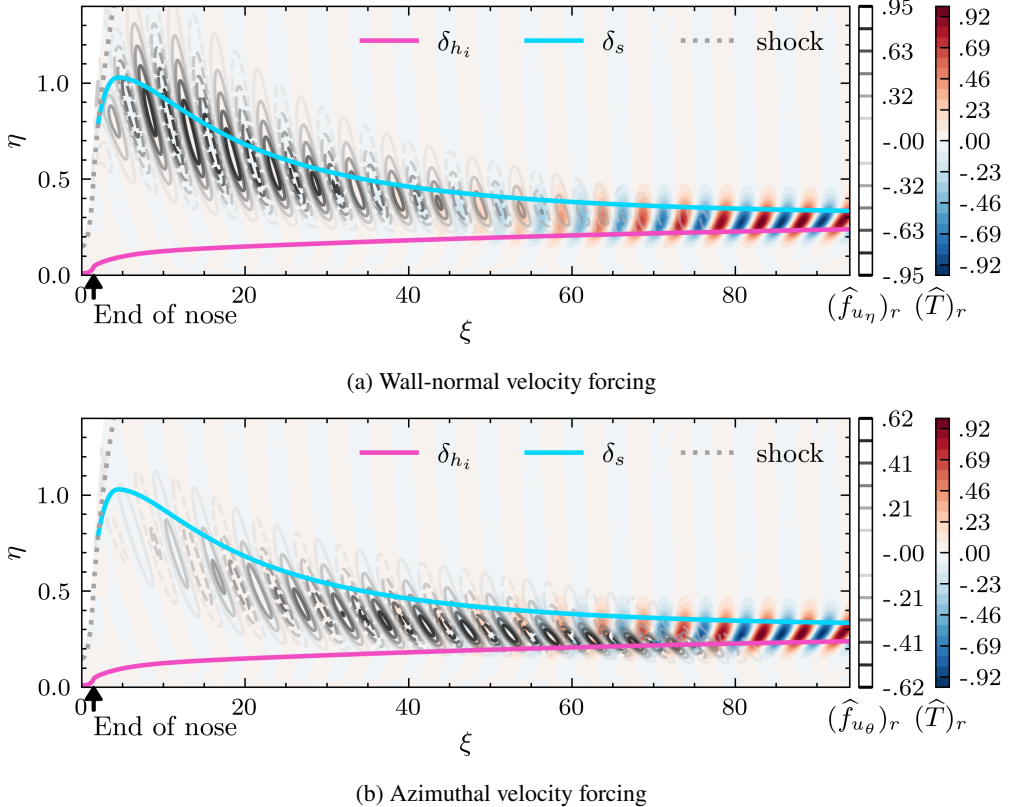


Figure 15: Global shape of the real parts of the azimuthal and wall-normal velocity forcing (grey lines, dashed lines are negative) and temperature response (blue) corresponding to variables with the largest amplitudes entropy layer mode. Normalised by $\max \|\hat{f}_u\|$ and $\max |\hat{T}|$ respectively

kinetic energy, up to $\xi = 15$, which is also where the local forcing is most important, but then quickly switches to being dominated by contributions from the temperature fluctuation T energy term in the Chu norm, until the end of the cone. At $\xi = 25$, the density D energy term also becomes more important than kinetic energy. This suggests that the forcing first excites velocity fluctuations in the entropy layer, and that there is a gradual transfer to density and temperature fluctuations. The response then peaks at $\xi = 86.4$ before the end of the domain, indicating that the mode is no longer able to grow once the entropy layer reaches some threshold of radial separation or parallelism with the boundary layer.

To understand how the mode is structured, Figures 15a and 15b show (ξ, η) streamwise planes for both wall-normal and azimuthal velocity forcing as well as the temperature response, which are the dominant primitive variables in the energy analysis. Figure 16 presents (θ, η) cross-sections showing, respectively, the forcing velocity field and the associated streamwise vorticity and the response velocity and temperature fields. For completeness, Figure 17 shows the forcing and response profiles at the same locations. A first consideration to note is that this mode has most of its forcing and response located far from the boundary layer, at the upper extremity of the entropy layer. However, when the entropy layer is less radially separated from the boundary layer, the forcing and the response also have some support at the top of the boundary layer. The forcing is primarily composed of

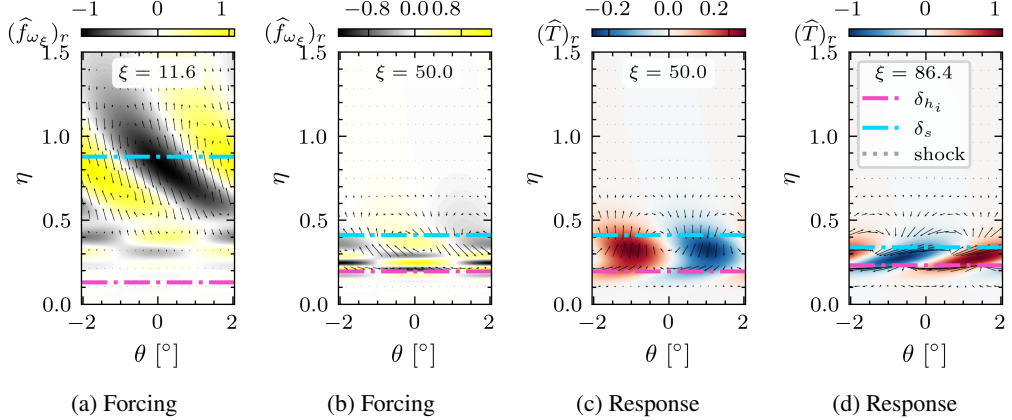


Figure 16: Real part of the forcing velocity vector field with associated streamwise vorticity (**left**) & real part of the response velocity and temperature (**right**) for the entropy layer mode

wall-normal velocity whose radial support extends beyond the entropy layer limit, according to the definition given in section 3. The forcing at these upstream positions is predominantly comprised of wall-normal velocity fluctuations of alternating sign (in θ and ξ). The associated streamwise vorticity forms bands with large azimuthal inclination. Downstream, after $\xi = 40$, azimuthal velocity forcing becomes more important and the forcing structure takes the form of a streamwise vortex, see also Figure 17b. The response emerges downstream as oscillating temperature in both the streamwise and azimuthal directions, with maximum support between the boundary and entropy layer edges. The forcing velocity structure is initially inclined against the velocity gradient, whereas the response structure becomes more and more inclined with the velocity gradient as it moves downstream. This gradual rotation of the structures from upstream to downstream is reminiscent of an Orr-like mechanism, it occurs here in the entropy layer rather than the boundary layer. The underlying cause may lie in the baseflow: between the boundary and entropy layer edges, the streamwise velocity continues to increase, forming a region of shear that convects the mode downstream with a velocity that varies with η within the entropy layer. In the azimuthal direction, the mode rotates clockwise, when $m > 0$, from upstream to downstream such that high temperature response zones are associated with upwards wall-normal velocity and inversely for cool temperature response zones such that high-temperature flow is lifted from the boundary layer into the entropy layer whereas low-temperature flow is drawn into the entropy layer from above.

6.2. Energy budget analysis of the entropy layer mode at $f^* = 35$ kHz, $m = 88$

To get a full picture of the mechanisms associated with this mode, an energy budget analysis is performed in a similar manner to that undertaken for the optimal streak mode. Figure 18a shows the most significant terms of kinetic energy production. The shear production term, is dominant everywhere and peaks around $\xi = 80$ shortly before the response Chu energy density maximum. Before it reaches the maximum production, there are two regions of exponential slope that can be identified. The first up to $\xi/Rn = 60$ where the slope is most important and a second after and up to the maximum at $\xi = 80$ where the slope is smaller. The beginning of this second zone, where the production is most important, matches the point at which the azimuthal velocity forcing becomes more important than the wall-normal velocity forcing, see Figure 14b.

To elucidate how the T energy grows, Figure 18b shows the different terms contributing to

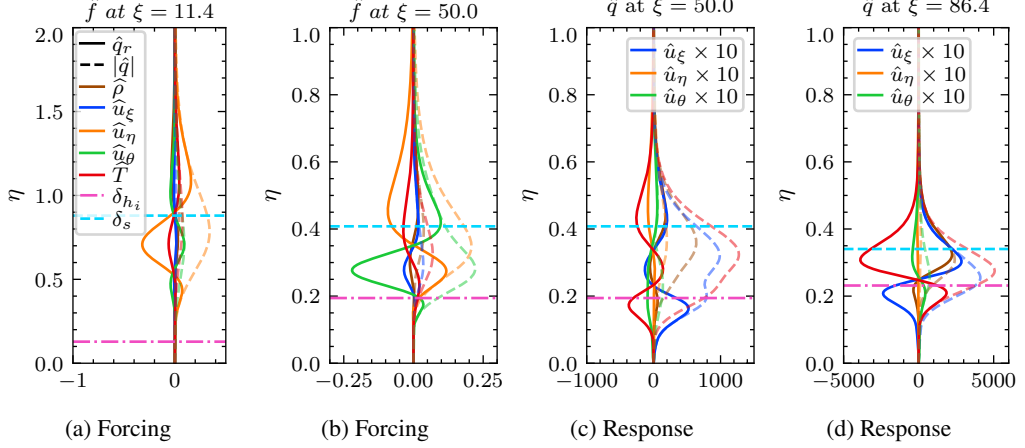


Figure 17: Non-dimensionalised local profiles of the entropy layer mode corresponding to the maximum forcing, an intermediate position and the maximum response curvilinear abscissa respectively

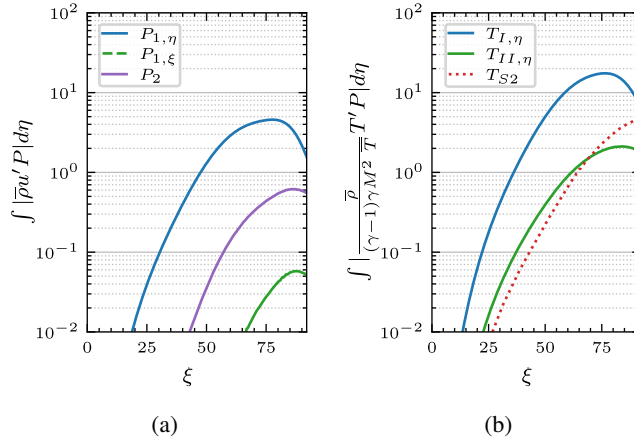


Figure 18: Wall-normal integrated dominant production terms for the linearised kinetic energy equation (left, 18a) and temperature equation (right, 18b) for the entropy layer mode

the T energy growth. It is the $T_{I,\eta}$ term, representing the transport of baseflow temperature by wall-normal velocity fluctuations, which dominates. The velocity dilatation is found not to play an important role in the growth of entropy layer modes. Though less pronounced than for the kinetic energy production, there are also two regions in the slope of the $T_{I,\eta}$ term. The first region up to $\xi = 60$, where the $T_{I,\eta}$ increases the most. Then the second region, between $\xi = 60$ up to the peak growth at $\xi = 80$, where the $T_{I,\eta}$ energy levels out.

These different elements suggest the following mechanism : entropy layer modes are produced by the combined action of velocity fluctuations and the baseflow temperature gradient, moving flow from regions of high to low energy. And, to a lesser measure, the action of the velocity fluctuations does the same to the momentum in the entropy layer.

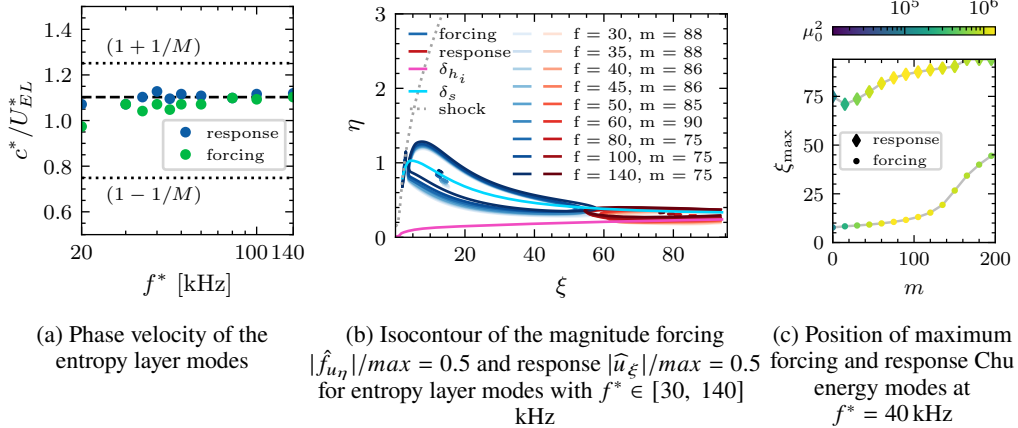


Figure 19

6.3. Entropy layer modes characteristics

We now consider the whole family of HAWEL modes with extensive support of both forcing and response in the entropy layer exists for a wide range of frequencies: from 20 to 140 kHz and azimuthal wavenumber between 75 and 90. The phase speed of the response modes, given by $c = \omega/\alpha$ where α is the streamwise (angular) wavenumber, is plotted in Figure 19a. This was computed using the streamwise wavenumber found by taking the dominant term of the spatial Fourier transform of $\hat{\mathbf{q}}$ on a wall-parallel line at $\eta/R_n = 0.3$. The resulting phase speed is found to be constant for the response modes at the optimal azimuthal wavenumber (following the black dots in Figure 4b) and is 1.09 times faster than the local flow velocity at the edge of the entropy layer at end of the domain. A similar method was used on the forcing modes and the phase velocity was found to be slightly lower in all cases.

The streamwise position of the maximum response E_η is independent of the frequency of the entropy layer mode considered. Additionally, the response and forcing outline in the (ξ, η) plane, shown in Figure 19b, is also independent of frequency for the optimal entropy layer modes, indicating a self-similarity of the entropy layer modes as function of frequency and a scaling that allows collapse of the mode shapes. However, when the azimuthal wavenumber differs significantly from the optimum, the streamwise position of peak forcing and response energy changes, see Figure 19c where the optimal forcing and response positions are provided and coloured by the optimal gain value. The streamwise position of maximum Chu energy density is here plotted for modes at 40 kHz as function of m . The position of the response continuously moves downstream as m increases in the range $m \in [40, 200]$ corresponding to entropy layer modes. This suggests that there is a characteristic length scale associated with the baseflow that defines the range of wavenumbers and frequencies of the entropy-layer modes. The forcing also follows the downstream trend of the peak with m , however the peak amplitude remains upstream until $m < 120$, then quickly move downstream for higher wavenumbers. This indicates that the forcing process primarily favours forcing where the radial separation between the boundary and entropy layer is high. Combined with the observation of a self-similarity of the mode organisation with frequency, this suggest that the characteristic time and length scales of these modes may be related to the height difference $\delta_s - \delta_{h_i}$ or the angles θ formed by the entropy and boundary layer $\theta(\delta_s) - \theta(\delta_{h_i})$. This scale could be a key parameter underpinning the receptivity of these modes.

7. Wall temperature effect : the adiabatic blunt cone

Past research on hypersonic boundary layer instabilities (Mack 1987) has shown a strong dependence of the classical Mack's 1st- and 2nd-modes amplification on the wall temperature to recovery temperature ratio (i.e. the adiabatic wall temperature). During hypersonic flight, the wall temperature can strongly vary depending on the material nature and the type of trajectories (reentry, cruise). Therefore the wall temperatures can evolve between cold to warm conditions motivating the study of the effects of the wall temperature to recovery temperature ratio. Hence, we now extend the analysis to a similar blunt cone configuration but with an adiabatic wall condition to compare it with the cold isothermal wall studied in the previous sections.

7.1. Resolvent gain maps

The optimal gain map for the adiabatic wall is shown in Figure 20. In contrast to the isothermal case, the most amplified mode is no longer the steady streak mode, but rather the first Mack mode, occurring at 15 kHz and azimuthal wavenumber $m = 23$. Such an amplification is consistent with the previously documented growth of first-mode instability for adiabatic to warm wall conditions (Mack 1987). This mode exhibits a gain of $\mu_0^2 = 1.48 \times 10^7 \text{ s}^2$, slightly exceeding the gain of $\mu_0^2 = 1.20 \times 10^7 \text{ s}^2$ observed for the isothermal streak mode but is greatly attenuated compared to the sharp case : $\mu_0^2 \approx 10^{11} \text{ s}^2$ for the 1st mode and $\mu_0^2 \approx 10^{13} \text{ s}^2$ for the 2nd mode. The significant gain separation between leading and first sub-optimal modes is consistent with a modal amplification mechanism. At low frequency, the most amplified streak mode in the adiabatic case is the steady mode at $m = 54$, with a gain of $1.28 \times 10^7 \text{ s}^2$. Beyond 35 kHz, the gain associated with the first Mack mode diminishes.

In this higher frequency range, a family of entropy layer modes re-emerges, displaying characteristics similar to those observed in the isothermal wall case. The gain and gain separation of the adiabatic entropy layer modes are similar to the isothermal case, indicating that these modes are not very sensitive to the wall condition. The shift in dominant amplification mechanisms between the isothermal and adiabatic wall conditions has practical implications for transition modelling on flight vehicles, for which the wall temperature may evolve between the colder isothermal wall and adiabatic wall cases.

7.2. Adiabatic blunt cone optimal 1st Mack mode

The most amplified adiabatic mode is the 1st Mack mode, which displays similar characteristics to the canonical sharp cone 1st Mack mode. A (ξ, η) streamwise plane of the mode is presented in Figure 21. The forcing and response is primarily located on the boundary layer limit. The optimal 1st Mack mode uses the Orr mechanism to maximise the initial perturbation energy. This is apparent in the receptivity structure that forms alternating bands inclined against the flow velocity gradient, characteristic of an Orr mechanism. Then the first-mode follows a modal exponential amplification as it evolves further downstream.

The presence of bluntness and the induced boundary layer causes the maximum gain of the 1st Mack mode to be greatly reduced in comparison with the flow over an equivalent sharp cone. However, the entropy layer does not modify the behaviour of the 1st Mack mode, and it is quite similar to that on a flat plate (Bugeat *et al.* 2019).

8. Conclusion

Transition over hypersonic moderately blunt bodies is not well understood and past research did not provide a comprehensive review of the instabilities and receptivity existing in such flows. The bluntness induces a detached shock which significantly alters the baseflow with

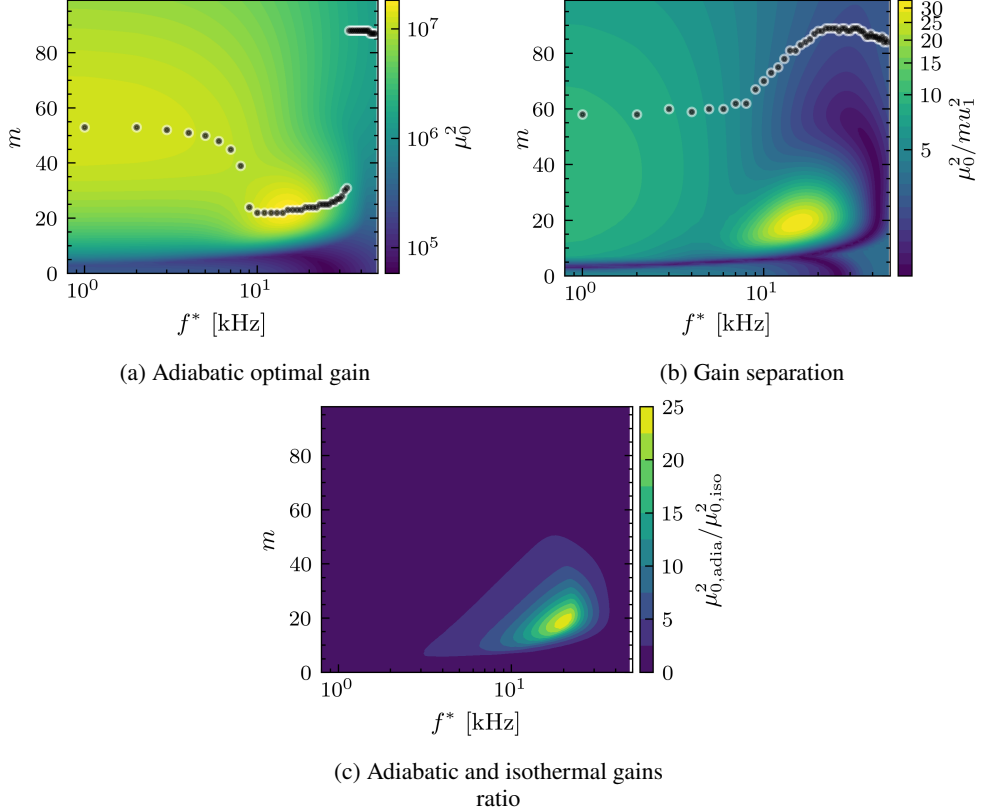


Figure 20: Adiabatic gain maps in the (f^*, m) plane. ● most amplified mode at given f^*

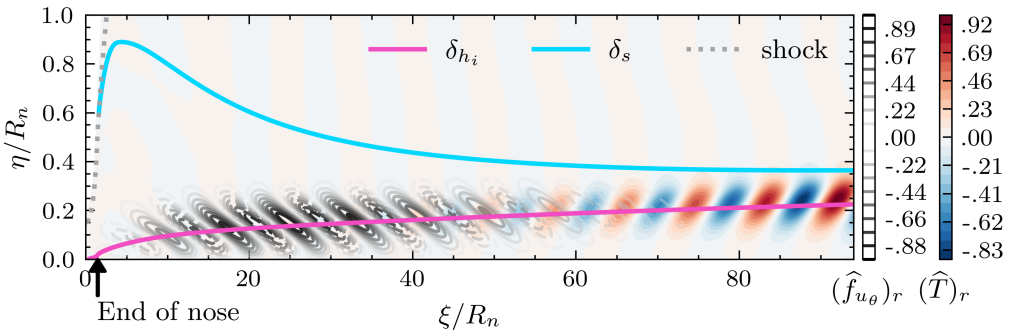


Figure 21: Global shape of the real parts of the azimuthal velocity forcing and temperature response of the adiabatic 1st Mack mode. Normalised by their respective maximum absolute value

respect to the sharp case, modifying the linear stability mechanisms responsible for transition. To tackle this problem, resolvent analysis was used for a 7° half-angle moderately blunt cone at Mach 6 with zero angle of attack and Reynolds number $Re_{R_n} = 90000$ in order to characterise, in a comprehensive manner, the linear amplification mechanisms that may arise for a large range of frequencies and wavenumbers. A general result is that at this intermediate Reynolds number, all Mack modes are strongly damped, especially the second mode, making

the path to transition unclear. Resolvent analysis shows that in the isothermal wall case, streak modes with azimuthal wavenumber $m = 57$ are the most amplified followed by a family of entropy layer modes at high azimuthal wavenumber (designated as HAWEL mode) with an amplification peak at $m \approx 88$. A last family of modes with a signature in the entropy layer, distinct from the HAWEL modes, has been identified at lower azimuthal wavenumbers ($m < 21$) (designated as LAWEL mode), and have a much smaller gain compared to other modes. One of the main result of this study lies in a first detailed description of these HAWEL optimal modes that are the leading amplification mechanisms for a large range of frequencies and wavenumbers. This descriptions is particularly useful as past hypersonic wind-tunnel experiments consistently displayed entropy-layer elongated fluctuations (wisps) in high-speed Schlieren imagery ([Marineau et al. 2014](#); [Jewell & Kimmel 2017](#); [Grossir et al. 2019](#); [Ceruzzi et al. 2024](#)). The key findings related to these instabilities is that they represent a family of modes with : a weak amplification (6 to 20 times less than steady streaks), a clear localisation of the optimal forcing in the entropy-layer far above the boundary-layer and an optimal response located in the entropy layer just above the boundary-layer after its starts merging with the entropy-layer. These modes are most susceptible to wall-normal velocity disturbances upstream which evolve downstream into alternating streamwise vorticity. The response on the other hand is most important on temperature fluctuations and an energy analysis shows that it is the conjoint action of wall-normal velocity fluctuations and wall-normal gradients of baseflow temperature and velocity which extract energy from the baseflow to the fluctuations.

Stationary streaks remain the most amplified mechanism, and may be expected to appear and participate in the transition process. Bluntness causes the receptivity region of streaks to move into the entropy layer compared to the sharp reference. The blunt optimal streak mode is most receptive to radial pumping before gradually entering the boundary layer, where the more usual streamwise vorticity appears in the forcing mode.

It is interesting to note that in both the HAWEL and streak-mode scenarios, the entropy layer plays a key role in the receptivity. Both of these modes are susceptible to wall-normal velocity forcing upstream in the entropy layer before becoming more susceptible to a longitudinal vortex structure forcing further downstream.

Modification of the baseflow by steady streaks changes the growth rate of modes ([Vaughan & Zaki 2011](#); [Caillaud et al. 2025a](#)). Studying the secondary stability problem would provide insight on possible transition scenarios. Furthermore, an interesting perspective would be to analyse the secondary stability problem of streaks associated with entropy layer modes.

Regarding the effect of wall conditions on the linear amplification mechanisms, this being important in understanding differences between real atmospheric re-entry and windtunnel testing, our study shows that in the case of an adiabatic wall condition, the 1st Mack mode becomes the most amplified mode in the (f^*, m) plane, followed by streaks and entropy layer modes at high azimuthal wavenumber. This further suggests that in moderately blunt regimes, the transition process may involve a competition between streaks, 1st Mack mode and entropy layer modes.

While the resolvent maps out all possible linear mechanisms and gives insight into optimal receptivity, it does not take into account the space of physical perturbations that are available to force the flow. Revisiting these findings with the physically realisable resolvent analysis developed by [Kamal et al. \(2023\)](#) will provide further clarification of how the amplification mechanisms identified and discussed in this paper are activated by atmospheric perturbations. Alternatively, with knowledge of the environmental disturbance, projection of these on the optimal resolvent basis would enable the calculation of a weighted optimal gain map, possibly highlighting new mechanisms.

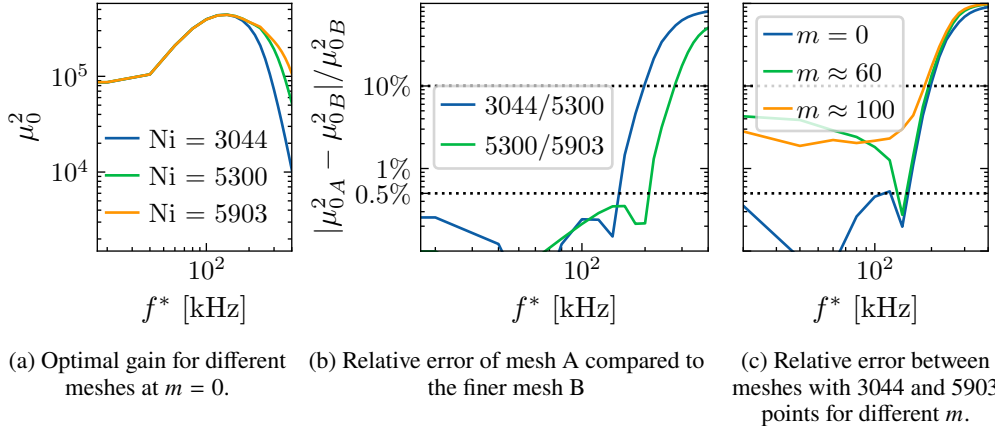


Figure 22

Finally, the transition process is not only a linear problem. Studying multimode transition scenarios will also be key in understanding the blunt cone transition process.

Declaration of interests. The authors report no conflict of interest

Appendix A.

A.1. Resolvent mesh convergence

The mesh convergence for the resolvent analysis is based on the convergence of the optimal gain. In figure 22, the optimal gain is plotted for different meshes with increasing streamwise resolution at $m = 0$. Only the streamwise resolution convergence is presented as the resolved wall-normal length-scale is much greater than that of the observed structures. Very good agreement is obtained for the roughest mesh with $Ni = 3044$ points in the streamwise direction until 150 kHz, where the relative error to the finer meshes crosses the 0.5% threshold. This mesh was used for all the analysis. The relative error increases to 10% above 200 kHz because the gain is underestimated, nonetheless, the trend is preserved and the mode structure is largely preserved.

The highest frequency necessary to resolve is that of the 2nd Mack mode. For the sharp case the 2nd mack mode becomes optimal at 300 kHz and peaks at 330 kHz. Based on the relation $f_{2^{nd}}^* \propto U_e/\delta$ the 2nd mode is expected to range from 240 to 260 kHz in the blunt case due to the thicker boundary layer. At these frequencies, the mesh with $Ni = 3044$ points is not well resolved but the 5300 mesh is with less than 10% error. There is no substantial increase in optimal gain as would be expected with the growth of the second Mack mode. Furthermore, looking at the profile of the mode obtained in this range of frequencies, it is clear that it does not correspond to the 2nd mode, see Figure 23. The 2nd Mack mode is truly attenuated to the point that it is no longer an optimal resolvent mode.

Appendix B. Profiles of suboptimal modes

To complete the discussion on suboptimal modes started in section 4.1 this Appendix presents additional profiles of the modes that were discussed.

In Figure 24 are presented the two first optimal and suboptimal modes at $m = 21$ at some key frequencies. At $f^* = 20$ kHz, we can observe that the forcing profile is characteristic of the 1st mode and is similar to what is observed for a flat plate (Bugeat *et al.* 2019). Between

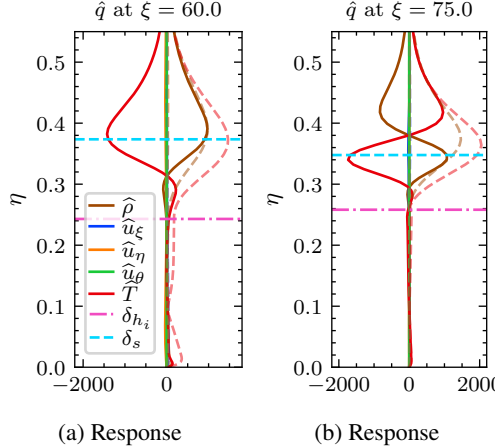


Figure 23: Optimal response of the mode $(f^*, m) = (260 \text{ kHz}, 0)$ computed with the high resolution mesh $Ni = 5903$ at two streamwise positions where the response is strong

$f^* = 20$ and 24 kHz , we can observe the switch in dominant mechanisms described based on the gains in Figure 7b. This is apparent by the switch in the shape of the forcing profiles where the optimal mode forcing at $f^* = 24 \text{ kHz}$ resembles closely to the suboptimal mode at $f^* = 20 \text{ kHz}$ and the characteristic shape of the 1^{st} mode appears in the suboptimal mode at $f^* = 24 \text{ kHz}$.

In section 4.1 was also mentioned the presence of axisymmetric shock modes at $m = 0$ and low frequencies. Here is an example in Figure 25 at $(f^*, m) = (1 \text{ kHz}, 0)$.

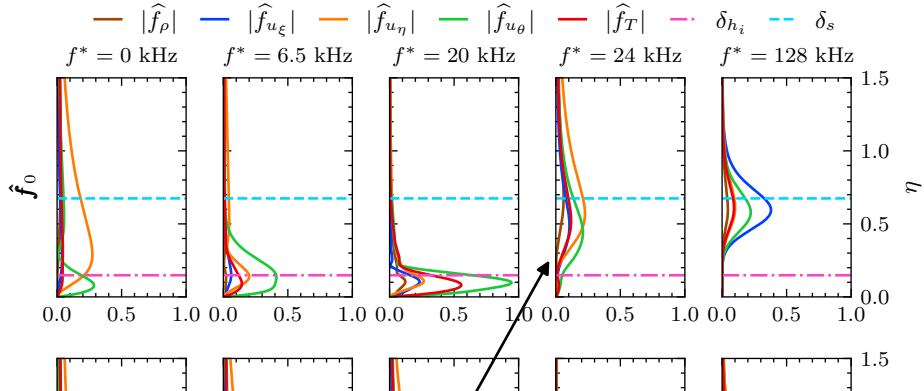
Appendix C. Linearised transport of streamwise velocity

The complete transport equations of velocity and temperature fluctuation used the energy budget performed in section 5 and 6.1 are given here in equations C 1 and C 2.

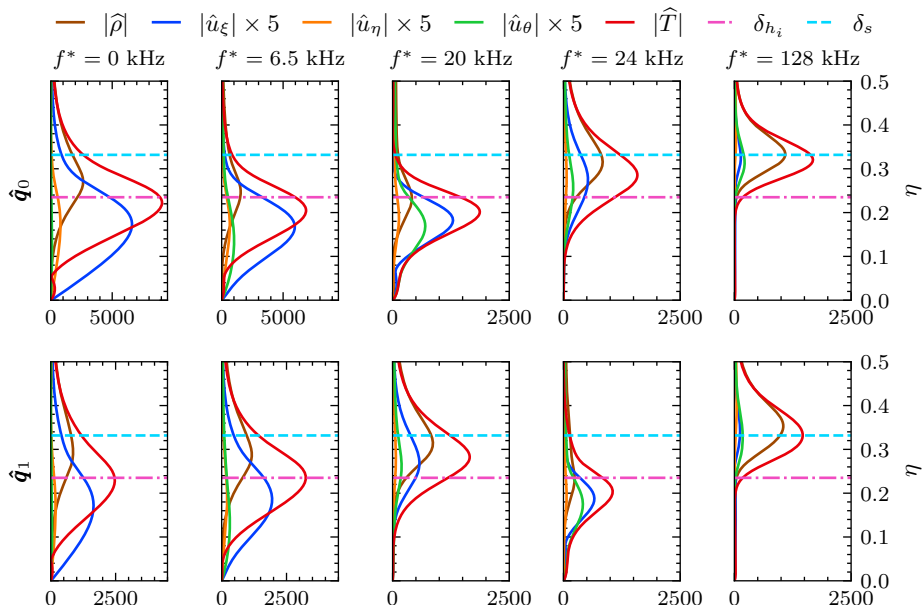
$$\partial_t \mathbf{u}' + (\bar{\mathbf{u}} \cdot \nabla) \mathbf{u}' = -(\mathbf{u}' \cdot \nabla) \bar{\mathbf{u}} - \frac{\rho'}{\bar{\rho}} (\bar{\mathbf{u}} \cdot \nabla) \bar{\mathbf{u}} - \frac{\nabla p'}{\bar{\rho}} + \frac{1}{\bar{\rho}} \nabla \cdot \boldsymbol{\tau}' + \frac{\mathbf{f}_{\rho \mathbf{u}}}{\bar{\rho}} \quad (\text{C } 1)$$

$$\begin{aligned} \partial_t T' + \bar{\mathbf{u}} \cdot (\nabla T') &= -\mathbf{u}' \cdot (\nabla \bar{T}) - \frac{\rho'}{\bar{\rho}} \bar{\mathbf{u}} \cdot (\nabla \bar{T}) \\ &\quad - \frac{\gamma - 1}{\gamma M_\infty^2} T' (\nabla \cdot \bar{\mathbf{u}}) + \frac{\gamma - 1}{\rho_\infty Re \bar{\rho}} (\nabla \bar{\mathbf{u}} : \boldsymbol{\tau}') + \frac{\gamma}{Pr Re \bar{\rho}} (\nabla \cdot (\bar{\mu} \nabla T')) \\ &\quad - \frac{\gamma - 1}{\gamma M_\infty^2} \bar{T} (\nabla \cdot \mathbf{u}') + \frac{\gamma - 1}{\rho_\infty Re \bar{\rho}} (\nabla \mathbf{u}' : \bar{\boldsymbol{\tau}}) + \frac{\gamma}{Pr Re \bar{\rho}} (\nabla \cdot (\mu' \nabla \bar{T})) \\ &\quad + \frac{\gamma M_\infty^2 (\gamma - 1)}{\bar{\rho}} (f_{\rho E} - \mathbf{f}_{\rho \mathbf{u}} \cdot \bar{\mathbf{u}}) \end{aligned} \quad (\text{C } 2)$$

To compute the production and source terms used in the energy budget analysis, we begin by multiplying Equation C 1 by $u_\xi' \mathbf{e}_\xi$ and Equation C 2 by T' . These equations are then respectively scaled by $\bar{\rho}$ and $\frac{\bar{\rho}}{(\gamma - 1) \gamma M_\infty^2 \bar{T}}$ to yield the terms that contribute to the Chu energy (see Equation 5.1). Finally, the wall-normal integral of the temporal and azimuthal mean is taken: $\langle \cdot \rangle = \frac{m f}{2\pi} \int_0^{\eta_{\max}} \int_0^{2\pi/m} \int_0^{1/f} \cdot dt d\theta d\eta$, when $m \neq 0$ and $f \neq 0$, otherwise the associated

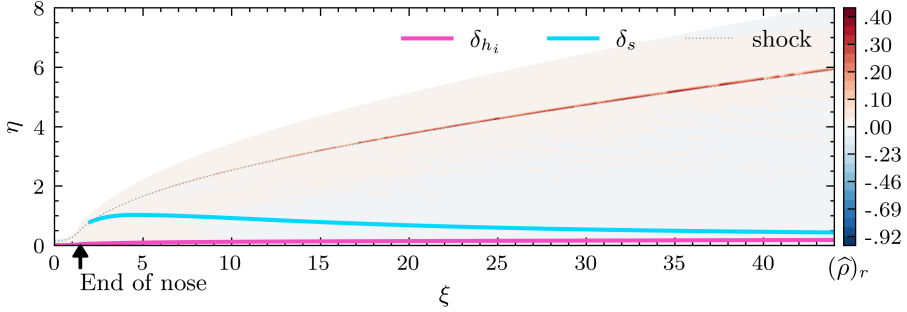


(a) Optimal forcing (top, mode 0) and 1st suboptimal response (bottom, mode 1) at $m = 21$ at $\xi = 20$



(b) Optimal response (top, mode 0) and 1st suboptimal response (bottom, mode 1) at $m = 21$ at $\xi = 94$

Figure 24

Figure 25: $(f^*, m) = (1 \text{ kHz}, 0)$ shock mode

mean is dropped. The complete equations are thus,

$$\bar{\rho} \partial_t \mathbf{u}' \cdot u_{\xi'} \mathbf{e}_{\xi} + \text{KE}_{\text{Tr}, \xi} = \text{KE}_{\text{P1}, \xi} + \text{KE}_{\text{P2}, \xi} + \text{KE}_{\text{S}, \xi} + \text{KE}_{\text{F}, \xi} \quad (5.2)$$

$$\begin{aligned} \frac{\bar{\rho}}{2(\gamma - 1)\gamma M_{\infty}^2 \bar{T}} \partial_t T'^2 + T_{\text{Tr}} = T_{\text{I}} + T_{\text{II}} + T_{\text{S1}} + T_{\text{V1}} + T_{\text{V}\mu 1} \\ + T_{\text{S2}} + T_{\text{V2}} + T_{\text{V}\mu 2} + T_{\text{F}} \end{aligned} \quad (5.3)$$

where,

$$\text{KE}_{\text{Tr}, \xi}(\xi) = \langle \bar{\rho} (\bar{\mathbf{u}} \cdot \nabla) \mathbf{u}' \cdot u_{\xi'} \mathbf{e}_{\xi} \rangle \quad (C 3)$$

$$\text{KE}_{\text{P1}, \xi}(\xi) = \langle -\bar{\rho} (\mathbf{u}' \cdot \nabla) \bar{\mathbf{u}} \cdot u_{\xi'} \mathbf{e}_{\xi} \rangle \quad (5.4)$$

$$\text{KE}_{\text{P2}, \xi}(\xi) = \langle -\rho' (\bar{\mathbf{u}} \cdot \nabla) \bar{\mathbf{u}} \cdot u_{\xi'} \mathbf{e}_{\xi} \rangle \quad (5.5)$$

$$\text{KE}_{\text{S}, \xi}(\xi) = \langle -\nabla p' \cdot u_{\xi'} \mathbf{e}_{\xi} \rangle \quad (C 4)$$

$$\text{KE}_{\text{V}, \xi}(\xi) = \langle \nabla \cdot \boldsymbol{\tau}' \cdot u_{\xi'} \mathbf{e}_{\xi} \rangle \quad (C 5)$$

$$\text{KE}_{\text{V}, \xi}(\xi) = \langle \mathbf{f}_{\rho \mathbf{u}} \cdot u_{\xi'} \mathbf{e}_{\xi} \rangle \quad (C 6)$$

$$T_{\text{T}}(\xi) = \left\langle \frac{\bar{\rho}}{(\gamma - 1)\gamma M_{\infty}^2 \bar{T}} \bar{\mathbf{u}} \cdot (\nabla T') T' \right\rangle \quad (C 7)$$

$$T_{\text{I}}(\xi) = \left\langle -\frac{\bar{\rho}}{(\gamma - 1)\gamma M_{\infty}^2 \bar{T}} \mathbf{u}' \cdot (\nabla \bar{T}) T' \right\rangle \quad (5.6)$$

$$T_{\text{II}}(\xi) = \left\langle -\frac{1}{(\gamma - 1)\gamma M_{\infty}^2 \bar{T}} \rho' \bar{\mathbf{u}} \cdot (\nabla \bar{T}) T' \right\rangle \quad (5.7)$$

$$T_{\text{S1}}(\xi) = \left\langle -\frac{\bar{\rho}}{\gamma^2 M_{\infty}^4} T' (\nabla \cdot \bar{\mathbf{u}}) T' \right\rangle \quad (C 8)$$

$$T_{\text{V1}}(\xi) = \left\langle \frac{1}{\gamma M_{\infty}^2 \bar{T} \rho_{\infty} Re} (\nabla \bar{\mathbf{u}} : \boldsymbol{\tau}') T' \right\rangle \quad (C 9)$$

$$T_{\text{V1}\mu}(\xi) = \left\langle \frac{1}{(\gamma - 1)M_{\infty}^2 \bar{T} Pr Re} (\nabla \cdot (\bar{\mu} \nabla T')) T' \right\rangle \quad (C 10)$$

$$T_{\text{S2}}(\xi) = \left\langle -\frac{\bar{\rho}}{\gamma^2 M_{\infty}^4} (\nabla \cdot \mathbf{u}') T' \right\rangle \quad (5.8)$$

$$T_{\text{V2}}(\xi) = \left\langle \frac{1}{\gamma M_{\infty}^2 \bar{T} \rho_{\infty} Re} (\nabla \mathbf{u}' : \bar{\boldsymbol{\tau}}) T' \right\rangle \quad (C 11)$$

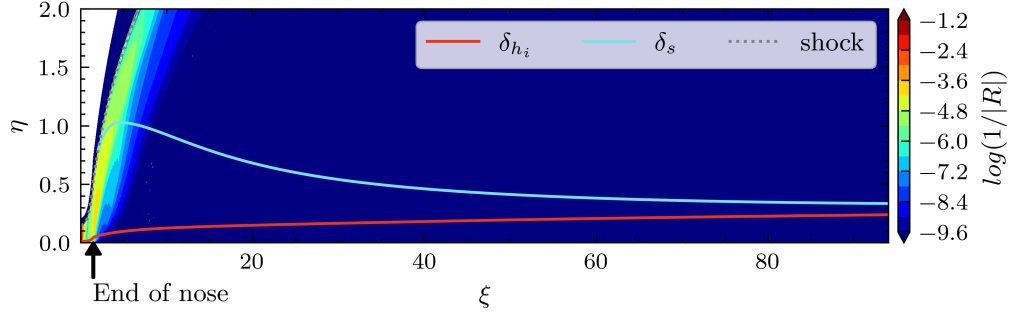


Figure 26: Inverse of the local radius of curvature of the flow

$$T_{V2\mu}(\xi) = \left\langle \frac{1}{(\gamma - 1)M_\infty^2 \bar{T} Pr Re} (\nabla \cdot (\mu' \nabla \bar{T})) T' \right\rangle \quad (C12)$$

$$T_F(\xi) = \left\langle \frac{1}{\bar{\rho}} (f_{\rho E} - f_{\rho \mathbf{u}} \cdot \bar{\mathbf{u}}) T' \right\rangle \quad (C13)$$

$$(C14)$$

Appendix D. Radius of curvature of the baseflow

The flow curvature can be determined based on the local flow velocity by:

$$R = \frac{|\mathbf{u}|^3}{u_\xi D_t u_\eta - u_\eta D_t u_\xi} \quad (D1)$$

where D_t is the material derivative. The inverse of the local radius of curvature of the flow is shown in Figure 26. The maximum flow curvature is $R > 10^{10} \approx 10^7$ m. The area of highest flow curvature is located near the stagnation point and at the start of the cone and has values of the order of $R \approx 100 \approx 0.5$ mm.

REFERENCES

BATISTA, ARMANI, KHAN, ARHAM AMIN & KUEHL, JOSEPH 2020 On the mechanism by which nose bluntness suppresses second-mode instability. *Theoretical and Applied Mechanics Letters* **10** (4), 230–240. 9

BUGEAT, B., CHASSAING, J.-C., ROBINET, J.-C. & SAGAUT, P. 2019 3D global optimal forcing and response of the supersonic boundary layer. *Journal of Computational Physics* **398**, 108888. 6, 23, 26

CAILLAUD, CLÉMENT, LEHNASCH, GUILLAUME, MARTINI, EDUARDO & JORDAN, PETER 2025a Effect of streaks on hypersonic boundary layer linear instability. *Physical Review Fluids* **10** (4), 043902. 25

CAILLAUD, CLÉMENT, SCHOLTEN, ANTON, KUEHL, JOSEPH, PAREDES, PEDRO, LUGRIN, MATHIEU, ESQUIEU, SÉBASTIEN, LI, FEI, CHOURHARI, MEELAN M., BENITEZ, ELIZABETH K., BORG, MATTHEW P., McDANIEL, ZACHARY A. & JEWELL, JOSEPH S. 2025b Separation and Transition on a Cone-Cylinder-Flare: Computational Investigations. *AIAA Journal* **63** (7), 2615–2634. 7

CERUZZI, ANDREW, LE PAGE, LAURENT, MCQUELLIN, LIAM P., CONDREN, WESLEY J. & MCGILVRAY, MATTHEW 2025 Observations of Boundary Layer Transition Reversal on a Blunt Cone in Hypersonic Flow. In *AIAA SCITECH 2025 Forum*. Orlando, FL: American Institute of Aeronautics and Astronautics. 2

CERUZZI, ANDREW, LE PAGE, LAURENT M., KERTH, PHILIPP, WILLIAMS, BENJAMIN A. & MCGILVRAY, MATTHEW 2024 Experimental investigation of boundary layer instabilities and transition on sharp and blunt cones in Oxford's High-Density Tunnel. In *AIAA SCITECH 2024 Forum*. Orlando, FL: American Institute of Aeronautics and Astronautics. 2, 3, 10, 25

CHU, BOA-TEH 1965 On the energy transfer to small disturbances in fluid flow (Part I). *Acta Mechanica* **1** (3), 215–234. [6](#)

COOK, DAVID A., THOME, JOHN, BROCK, JOSEPH M., NICHOLS, JOSEPH W. & CANDLER, GRAHAM V. 2018 Understanding effects of nose-cone bluntness on hypersonic boundary layer transition using input–output analysis. In *2018 AIAA Aerospace Sciences Meeting*. Kissimmee, Florida: American Institute of Aeronautics and Astronautics. [2](#)

DEFENSE SCIENCE BOARD WASHINGTON DC 1988 Report of the Defense Science Board Task Force on the National Aerospace Plane (NASP).: *Tech. Rep.*. Defense Technical Information Center, Fort Belvoir, VA. [2](#)

DWIVEDI, ANUBHAV, SIDHARTH, G. S., NICHOLS, JOSEPH W., CANDLER, GRAHAM V. & JOVANOVIĆ, MIHAJLO R. 2019 Reattachment streaks in hypersonic compression ramp flow: an input–output analysis. *Journal of Fluid Mechanics* **880**, 113–135. [16](#)

GROSSIR, GUILLAUME, PINNA, FABIO & CHAZOT, OLIVIER 2019 Influence of Nose-Tip Bluntness on Conical Boundary-Layer Instabilities at Mach 10. *AIAA Journal* **57** (9), 3859–3873, publisher: American Institute of Aeronautics and Astronautics .eprint: <https://doi.org/10.2514/1.J057822>. [3](#), [10](#), [25](#)

HARTMAN, ANDREW B., HADER, CHRISTOPH & FASEL, HERMANN F. 2021 Nonlinear transition mechanism on a blunt cone at Mach 6: oblique breakdown. *Journal of Fluid Mechanics* **915**, R2. [3](#), [18](#)

HASCOET, LAURENT & PASCUAL, VALÉRIE 2013 The Tapenade Automatic Differentiation tool: principles, model, and specification. *ACM Transactions on Mathematical Software* **39** (3), publisher: Association for Computing Machinery. [7](#)

JEWELL, JOSEPH S., KENNEDY, RICHARD E., LAURENCE, STUART J. & KIMMEL, ROGER L. 2018 Transition on a Variable Bluntness 7-Degree Cone at High Reynolds Number. In *2018 AIAA Aerospace Sciences Meeting*. Kissimmee, Florida: American Institute of Aeronautics and Astronautics. [2](#), [4](#)

JEWELL, JOSEPH S. & KIMMEL, ROGER L. 2017 Boundary-Layer Stability Analysis for Stetson's Mach 6 Blunt-Cone Experiments. *Journal of Spacecraft and Rockets* **54** (1), 258–265. [25](#)

KAMAL, OMAR, LAKEBRINK, MATTHEW T. & COLONIUS, TIM 2023 Global receptivity analysis: physically realizable input–output analysis. *Journal of Fluid Mechanics* **956**, R5. [18](#), [25](#)

KENNEDY, RICHARD E., JAGDE, ERIC K., LAURENCE, STUART J., JEWELL, JOSEPH S. & KIMMEL, ROGER L. 2019 Visualizations of Hypersonic Boundary-Layer Transition on a Variable Bluntness Cone. In *AIAA Aviation 2019 Forum*. Dallas, Texas: American Institute of Aeronautics and Astronautics. [3](#)

KENNEDY, RICHARD E., JEWELL, JOSEPH S., PAREDES, PEDRO & LAURENCE, STUART J. 2022 Characterization of instability mechanisms on sharp and blunt slender cones at Mach 6. *Journal of Fluid Mechanics* **936**, A39. [3](#), [4](#), [10](#), [18](#)

LANDAHL, M. T. 1980 A note on an algebraic instability of inviscid parallel shear flows. *Journal of Fluid Mechanics* **98** (2), 243–251. [16](#)

LEI, JIA & ZHONG, XIAOLIN 2012 Linear Stability Analysis of Nose Bluntness Effects on Hypersonic Boundary Layer Transition. *Journal of Spacecraft and Rockets* **49** (1), 24–37. [2](#), [9](#)

MACK, LESLIE 1987 Stability of axisymmetric boundary layers on sharp cones at hypersonic Mach numbers. In *19th AIAA, Fluid Dynamics, Plasma Dynamics, and Lasers Conference*. Honolulu, HI, U.S.A.: American Institute of Aeronautics and Astronautics. [2](#), [3](#), [23](#)

MARINEAU, ERIC C., MORARU, GEORGE C., LEWIS, DANIEL R., NORRIS, JOSEPH D., LAFFERTY, JOHN F., WAGNILD, ROSS M. & SMITH, JUSTIN A. 2014 Mach 10 Boundary Layer Transition Experiments on Sharp and Blunted Cones (Invited). In *19th AIAA International Space Planes and Hypersonic Systems and Technologies Conference*. Atlanta, GA: American Institute of Aeronautics and Astronautics. [2](#), [9](#), [25](#)

PAREDES, PEDRO, CHOUDHARI, MEELAN M. & LI, FEI 2017 Blunt-body paradox and transient growth on a hypersonic spherical forebody. *Physical Review Fluids* **2** (5), 053903. [2](#)

PAREDES, PEDRO, CHOUDHARI, MEELAN M. & LI, FEI 2020 Mechanism for frustum transition over blunt cones at hypersonic speeds. *Journal of Fluid Mechanics* **894**, A22. [2](#), [3](#), [18](#)

PAREDES, PEDRO, CHOUDHARI, MEELAN M., LI, FEI, JEWELL, JOSEPH S. & KIMMEL, ROGER L. 2019a Nonmodal Growth of Traveling Waves on Blunt Cones at Hypersonic Speeds. *AIAA Journal* **57** (11), 4738–4749, publisher: American Institute of Aeronautics and Astronautics .eprint: <https://doi.org/10.2514/1.J058290>. [2](#), [10](#)

PAREDES, PEDRO, CHOUDHARI, MEELAN M., LI, FEI, JEWELL, JOSEPH S., KIMMEL, ROGER L., MARINEAU, ERIC C. & GROSSIR, GUILLAUME 2019b Nose-Tip Bluntness Effects on Transition at Hypersonic Speeds. *Journal of Spacecraft and Rockets* **56** (2), 369–387. [2](#), [8](#)

POULAIN, ARTHUR, CONTENT, CEDRIC, SIPP, DENIS, RIGAS, GEORGIOS & GARNIER, ERIC 2023 BROADCAST:

A high-order compressible CFD toolbox for stability and sensitivity using Algorithmic Differentiation. *Computer Physics Communications* **283**, 108557, arXiv:2206.05493 [physics]. [7](#)

RESHOTKO & TUMIN 2004 Role of Transient Growth in Roughness-Induced Transition. [2](#)

ROSENBOOM, I., HEIN, S. & DALLMANN, U. 1999 Influence of nose bluntness on boundary-layer instabilities in hypersonic cone flows. In *30th Fluid Dynamics Conference*. Norfolk, VA, U.S.A.: American Institute of Aeronautics and Astronautics. [2](#)

SCHMID, PETER J. 2007 Nonmodal Stability Theory. *Annual Review of Fluid Mechanics* **39** (1), 129–162. [6](#)

STETSON, K., THOMPSON, E., DONALDSON, J. & SILER, L. 1983 Laminar boundary layer stability experiments on a cone at Mach 8. I - Sharp cone. In *16th Fluid and Plasmadynamics Conference*. Danvers, MA, U.S.A.: American Institute of Aeronautics and Astronautics. [2](#)

TOWNE, AARON, SCHMIDT, OLIVER T. & COLONIUS, TIM 2018 Spectral proper orthogonal decomposition and its relationship to dynamic mode decomposition and resolvent analysis. *Journal of Fluid Mechanics* **847**, 821–867. [6](#)

VAUGHAN, NICHOLAS J. & ZAKI, TAMER A. 2011 Stability of zero-pressure-gradient boundary layer distorted by unsteady Klebanoff streaks. *Journal of Fluid Mechanics* **681**, 116–153. [25](#)